Long-term precision editing of neural circuits in mammals using engineered gap junction hemichannels

Elizabeth Ransey[1,2], Kirill Chesnov[1,3], Gwenaëlle E. Thomas[1,3], Elias Wisdom[6], Ryan Bowman[2], Tatiana Rodriguez[2], Elise Adamson[1,5], Agustin Almoril-Porras[6], Kathryn K. Walder-Christensen[1,2], Dalton Hughes[1,3], Hannah Schwennesen[2], Stephen D. Mague[1,2], Daniel Colón-Ramos [6,7], Rainbo Hultman[8], Nenad Bursac[5], Kafui Dzirasa[1,2,3,4,5,9]

[1]Howard Hughes Medical Institute, Chevy Chase, Maryland 20815, USA; [2]Dept. of Psychiatry and Behavioral Sciences, [3]Dept. of Neurobiology, [4]Dept. of Neurosurgery, Duke University Medical Center, Durham, North Carolina 27710, USA; [5]Dept. of Biomedical Engineering, Duke University, Durham North Carolina 27708, USA; [6]Department of Neuroscience and Department of Cell Biology, Program in Cellular Neuroscience, Neurodegeneration and Repair, Yale University School of Medicine, New Haven, CT, USA; [7]Instituto de Neurobiología, Recinto de Ciencias Médicas, Universidad de Puerto Rico, San Juan, Puerto Rico; [7]Department of Molecular Physiology and Biophysics, Department of Psychiatry, University of Iowa, Iowa City, IA, 52242 USA

[9]Lead Contact

*Correspondence:
Email: kafui.dzirasa@duke.edu
Twitter: @KafuiDzirasa

Summary

The coordination of activity between brain cells is a key determinant of neural circuit function; nevertheless, approaches that selectively regulate communication between two distinct cellular components of a circuit, while leaving the activity of the presynaptic brain cell undisturbed remain sparse. To address this gap, we developed a novel class of electrical synapses by selectively engineering two connexin proteins found in *Morone americana* (white perch fish): connexin34.7 (Cx34.7) and connexin35 (Cx35). By iteratively exploiting protein mutagenesis, a novel *in vitro* assay of connexin docking, and computational modeling of connexin hemichannel interactions, we uncovered the pattern of structural motifs that broadly determine connexin hemichannel docking. We then utilized this knowledge to design Cx34.7 and Cx35 hemichannels that dock with each other, but not with themselves nor with other major connexins expressed in the mammalian central nervous system. We validated these hemichannels *in vivo* using *C. elegans* and mice, demonstrating that they can facilitate communication across neural circuits composed of pairs of genetically distinct cell types and modify behavior accordingly. Thus, we establish a potentially translational approach, 'Long-term integration of Circuits using connexins' (LinCx), for context-precise circuit-editing with unprecedented spatiotemporal specificity in mammals.

Keywords: circuit editing; connexins; docking; behavior; neuromodulation; electrical synapses

Introduction

Many molecular events at synapses regulate the communication between cells, and studies have linked changes in synchrony across brain circuits to cognitive and emotional behaviors. For example, electrical oscillations in hippocampus and prefrontal cortex synchronize during spatial memory in rats [1], and between amygdala and hippocampus during fear memory retrieval in mice [2]. Moreover, altered long range synchrony has been observed in preclinical rodent models of schizophrenia [3], depression [4], and autism [5], and manipulating synchrony between infralimbic cortex and thalamus has been shown to enhance resilience to acute stress [6]. Though these studies highlight the therapeutic potential for modulating synchrony to drive long lasting changes in behavior, it remains a major challenge to manipulate the activity of precise brain circuits with sufficient precision to elicit synchrony. Both spatial (i.e., the interaction of specific cells in space) and temporal constraints of endogenous neural circuits (i.e., the ongoing integrated activity across multiple circuits) make this goal especially challenging. For example, classic pharmacological therapeutics targeting ion receptors or neuromodulatory pathways impact many brain circuits, and emerging brain stimulation-based approaches directly impact the activity of many neuronal populations (i.e., the rate code) and the timing of activity between distinct cells that comprise neural circuits (i.e., the timing code as reflected by synchrony). As such, tools that selectively regulate synchrony within specific circuits in animals have been sparse.

Gap junctions (electrical synapses) enable direct flow of ions and small molecules between two cells and play a prominent role in broadly synchronizing electrical activity in many organs such as the heart and the brain [7]. To achieve such synchrony, gap junction consists of two docked segments called hemichannels, embedded in the membranes of two adjoining cells. Each hemichannel, in turn, is an oligomer consisting of six monomeric proteins called connexins (Cx), of which there are 21 isoforms in humans [8, 9]. Most Cxs can form single-isoform hemichannels that dock with themselves to create homotypic gap junctions (Fig. 1A, left). This common feature limits the potential utility of Cxs as tools to

selectively regulate brain circuit activity in complex organisms. Expression of ectopic Cx proteins that form homotypic synapses would establish connections between individual neurons of the same cell type, though they may operate in distinct neural circuits (Fig. 1A, left). In such a scenario, information would flow simultaneously across otherwise independent circuits. On the other hand, several Cx hemichannels are capable of recognizing hemichannels composed of other Cx protein isoforms and can generate heterotypic, gap junctions (Fig 1A, right) [10, 11]. Thus, we reasoned that an exclusively heterotypic hemichannel pairing would provide substantial control over the direction of information flow between distinct cell types, and that mechanistic characterization of homotypic and heterotypic hemichannel docking may support the rational design of such a pair (Fig. 1A). We also reasoned that knowledge of these mechanisms docking could be utilized to engineer connexin proteins that were docking incompetent to the major connexins endogenous to the mammalian CNS, a feature that would be essential for any tools developed for precise circuit editing in mammalian species.

Morone americana (white perch fish) expresses two homologs of mammalian neuronal connexin36 (Cx36) – Cx34.7 and Cx35 – that create heterotypic electrical synapses between auditory afferents and Mauthner cells in the CNS [12]. Critically, the Cx34.7/Cx35 heterotypic gap junction exhibits rectification in the Cx34.7 to Cx35 direction [12], with an intrinsic conductance that increases above the threshold (i.e., -20mV) for action potential firing in the brains of mammals [13]. Since this former feature of the Cx34.7/Cx35 heterotypic gap junction enables a preferred directional modulation that parallels the general operation of chemical synapses, we chose Cx34.7 and Cx35 as our platform to engineer the desired features of a novel synthetic electrical synapse. We systematically mutated the residues responsible for Cx34.7 and Cx35 docking to generate two mutant hemichannels that exhibit heterotypic but not homotypic interactions, and do not dock with other connexin proteins endogenous to the mammalian CNS. We then deployed this synthetic synapse in C. elegans and mice to demonstrate its functionality and specificity as a neuronal circuit editing tool.

Results

In vitro analysis of connexin protein docking

Though the precise interactions that guide hemichannel docking are incompletely characterized for the majority of connexins, structure–function and sequence analyses indicate that the second extracellular loop (EL2) plays the greatest role in hemichannel docking specificity [14]. We developed an *in vitro* approach for rapid evaluation of connexin hemichannel docking [15]. Here, we reasoned that this approach could be used to rapidly screen a library of mutations for their ability to disrupt homotypic docking for the two mutants. Subsequently, a subset of non-homotypic docking Cx34.7 and Cx35 mutants could be screened against each other to identify putative heterotypic docking pairs.

Our rapid screening approach, Flow cytometry Enabled Tracking of Connexosomes in HEK cells (FETCH), enables rapid assessment of docking for many combinations of connexin proteins using flow cytometry. Specifically, FETCH utilizes the presence of connexosomes (a by-product of gap junction formation) as an indicator of docking compatibility. Connexosomes are double-bilayer, vesicular structures composed of fully-docked gap junctions that are internalized into each cell contributing to gap junctions as part of normal turnover (Fig. 1B)[16, 17]. Thus, docking compatibility of different fluorescently-labeled Cxs can be characterized as a function of the fluorescence exchange between cells, mediated by connexosomes [15]. In our assay, individual Cxs are expressed as either GFP- or RFP670-fluorescent fusion proteins in HEK cells. Following an initial expression, HEK cells that are expressing intended Cx counterparts are then co-plated and incubated. This allows apposed Cxs to potentially interact, and fluorescence exchange is subsequently evaluated using flow cytometry. Docking is characterized as the proportion of dual-labeled fluorescent cells that develop in a co-plated sample.

To identify potential mutations that destabilize Cx34.7 and Cx35 homotypic hemichannel docking, we rationally introduced seventy and sixty-seven mutations at sixteen positions on both extracellular loops

(ELs) of Cx34.7 and Cx35, respectively (see methods for mutant library design; Fig 1C). We then quantified homotypic docking interactions of these mutant proteins using FETCH screening (Fig. 1D and 1E). Here, our goal was to identify residues that completely disrupted docking; thus, we benchmarked the mutant scores against a heterotypic pairing of human Cx36 and Cx45 proteins that has previously been shown not to yield functional gap junctions [18]. Critically, for this screening, we were agnostic as to whether these mutations directly disrupted docking interactions or indirectly disrupted docking via interference with an upstream process such as folding or trafficking. Homotypic FETCH screening revealed that most mutants retained their docking character; however, several non-homotypic docking mutant proteins were identified. Non-homotypic Cx34.7 mutants included Y78S, Y78T, Y78V, E225K, E225R, L238Y and K222Q, and non-homotypic Cx35 mutants included N56E, Y78V, Y78S, Y78T, E224H, E224K, E224R, and L237Y (Fig. 1D and 1E)

Next, to identify mutant protein pairs that exhibit exclusively heterotypic docking, we screened the Cx34.7 and Cx35 non-homotypic mutants against each other using FETCH. Here, a successful docking interaction verified that upstream process such as folding or trafficking remained intact for both Cx mutants. Strikingly, we discovered three connexin mutant pairs whose FETCH scores were higher than the FETCH scores observed for wild type $Cx34.7_{WT}/Cx35_{WT}$ gap junctions. These results provided clear evidence that it was indeed feasible to engineer a connexin hemichannel pairs that demonstrated heterotypic, but not homotypic, docking. Interacting mutant pairs were comprised of $Cx34.7_{K222Q}$ with either $Cx35_{E224H}$, $Cx35_{E224K}$, or $Cx35_{E224R}$ as counterparts (Fig. 1F).

Since our long-term objective was to develop a modulation approach that would be amenable for use in the mammalian nervous system, we also probed whether the four mutant isoforms docked with endogenous connexin isoforms– specifically Cx36 and connexin43 (Cx43), the major connexins in mammalian neurons and astrocytes, respectively [19, 20]. Using heterotypic FETCH analysis, we observed that none of the mutant proteins interacted with human Cx43 (FETCH=1.3±0.1%; T_{96}=0.29;

P=0.61 for $Cx34.7_{K222Q}$/Cx43 compared to established non-docking pair replicates using a one tailed t-test, with a Bonferroni correction for 20 comparisons; FETCH=0.4±0.1%, 0.5±0.1%, and 0.5±0.1%; T_{96}= 1.41, 1.36, and 1.28; P=0.92, 0.91 and 0.90 for $Cx35_{E224H}$,/Cx43, $Cx35_{E224K}$/Cx43, and $Cx35_{E224R}$/Cx43, respectively; N=6 replicates for all experimental connexin pairs; FETCH=1.5±0.2%, N=92 for established non-docking pairs; see methods). However, $Cx34.7_{K222Q}$ and $Cx35_{E224H}$ interacted and formed heterotypic gap junctions with human Cx36 (FETCH=22.8±1.9%; T_{91}=-24.4; P=3.4×10^{-43} for $Cx34.7_{K222Q}$/Cx36; FETCH=5.9±1.1%, 0.8±0.1%, and 0.6±0.1%; T_{96}=-5.50, 0.89, and 1.24; P=1.6×10^{-7}, 0.81, and 0.89 for $Cx35_{E224H}$/Cx36, $Cx35_{E224K}$/Cx36, $Cx35_{E224R}$/Cx36, respectively).

Rational design of exclusively heterotypic and mammalian orthogonal Cx34.7 and Cx35 pair using *in silico* modeling

To address the unintended docking of $Cx34.7_{K222Q}$ with Cx36 determined via FETCH, we utilized homology modeling to rationally design a heterotypically exclusive connexin pair that does not interact with endogenous Cx43 and Cx36. Briefly, we first developed computational models of the Cx34.7 and Cx35 wild type and mutant, homotypic and heterotypic gap junctions that we had tested in the initial FETCH screen. We then validated the computational model by comparing the key residues predicted to underly hemichannel docking against the initial docking characteristics of the mutants we determined using FETCH. Next, we modeled the docking interactions between $Cx34.7_{K222Q}$, $Cx35_{E224H,}$ $Cx35_{E224K,}$ and $Cx35_{E224R}$ mutant proteins and Cx36. Finally, we utilized the insights of residue-wise interaction models to design Cx34.7 and Cx35 hemichannels that would exhibit exclusively heterotypic docking and would not dock with Cx36 or Cx43. We confirmed the docking characteristics of our designer Cx34.7 and Cx35 proteins *in vitro* using FETCH (Fig. 2).

Specifically, to model docking interactions between Cx34.7 and Cx35 gap junctions, we ran molecular dynamics simulations of modeled homotypic and heterotypic pairs of wild type and mutant proteins

(Cx34.7 and Cx35). Our modeling revealed large negative interaction energies involving residues E214, K222, E223, and E225 in wild type Cx34.7 and residues E213, K221, D222, E224 in wild type Cx35 for both the homotypic and heterotypic docking simulations. These large negative interaction energies were suggestive of salt bridges that stabilize both homotypic and heterotypic docking interactions, since results from our initial homotypic FETCH screens showed that mutations at positions Cx34.7-K222 and Cx35-E224 disrupted docking. Providing further support for this interpretation, residues in EL2 that had the lowest interaction energies in the wild type pairs showed much higher energy in mutants for which the charge was switched (e.g., $Cx35_{D222H}$, $Cx35_{D222R}$, $Cx35_{E224R}$, and $Cx34.7_{E223K}$), or for which a smaller residue of the same charge was introduced (e.g., $Cx34.7_{K222H}$). Integrating these results, we defined a common interaction motif for both Cx34.7 and Cx35 consisting of three negative residues (E214/E213, E223/D222, and E225/E224 for Cx34.7 and Cx35, respectively), and a positive residue (K222/K221 for Cx34.7 and Cx35, respectively, see Fig. 3). Thus, we determined that the four residues indeed play a prominent role in docking interactions for wild type homotypic and heterotypic Cx34.7 and Cx35 gap junctions.

Next, we introduced Cx36 into our computational modeling pipeline to characterize its homotypic and heterotypic interaction principles. Upon simulating the homotypic Cx36 gap junction, we determined the same pattern of interactions observed for Cx34.7 and Cx35, with residues E230, K238, E239, and E241 serving as key interaction sites. Given that the predicted Cx36 interaction motif is identical to that of Cx34.7, it is unsurprising that Cx36 was additionally modeled to interact with Cx34.7 and Cx35 heterotypically. After verifying these heterotypic docking interactions via FETCH (FETCH=11.9±1.2%; T_{96} =-12.93; P=4.7×10^{-23} for Cx34.7/Cx36; FETCH=18.0±2.0%; T_{96}=-18.69; P =4.7×10^{-34} for Cx35/Cx36), we introduced the four Cx mutants identified in our initial FETCH analysis ($Cx34.7_{K222Q}$, $Cx35_{E224H}$, $Cx35_{E224K}$, $Cx35_{E224R}$) into our computational framework and modelled their modified heterotypic interactions with Cx36.

Mutating K222Q in Cx34.7 disrupted the large negative interaction energies we observed in the homotypic wild type Cx34.7 model, consistent with our findings from FETCH analysis that this mutation impaired homotypic docking (FETCH=0.4±0.1%; T_{96}=1.43; P=0.92 homotypic Cx34.7$_{K222Q}$). On the other hand, the three negative residues in Cx34.7$_{K222Q}$ continued to show large negative interaction energies with the positive residue of Cx36, explaining the preserved heterotypic docking between Cx34.7$_{K222Q}$ and Cx36 observed via FETCH. Screened mutant Cx35 proteins (Cx35$_{E224H}$, Cx35$_{E224K}$, and Cx35$_{E224R}$) maintained the positive K221 residue that formed strong interactions with the negative residues of Cx36; however, the Cx35$_{E224K}$, and Cx35$_{E224R}$ mutations induced strong repulsion with the positive K238 residue of Cx36, explaining why these two mutants failed to heterotypically dock with Cx36 in our FETCH analyses. Interestingly, introducing a smaller positive charge at the same position, Cx35$_{E224H}$ restored the interaction with Cx36 in the computational model, and docking in our heterotypic FETCH analyses.

Having determined putative interaction principles underlying the docking of the three connexin homologs (Cx34.7, Cx35, and Cx36), we set out to rationally design a Cx34.7/Cx35 pair that would exhibit isoform-specific, exclusively heterotypic docking. Our initial strategy was to mutate residues at the four positions of our identified docking motif such that one connexin isoform contained all negatively charged interactors, and the counterpart connexin contributed all positively charged interactors. Cx35$_{K221E}$ (all negative charges at motif residues) showed strong repulsions in our homotypic model, and it did not exhibit homotypic docking in FETCH analysis (FETCH=1.2±0.4%; T_{96}=0.35; P=0.64). Additionally, this mutant protein failed to dock with Cx36 and Cx43 (FETCH=1.5±0.1%, T_{91}=0.02, P=0.51 and 1.7±0.2, T_{96}=-0.32, P=0.37 for Cx35$_{K221E}$/Cx36 and Cx35$_{K221E}$/Cx43, respectively). Similarly, Cx34.7$_{E214K/E223K/E225K}$ (all positive charges at motif residues) showed strong repulsions in our homotypic computation model and did not exhibit homotypic docking in FETCH analysis (FETCH=0.2±0.0%; T_{96}=1.76; P=0.96). However, when Cx35$_{K221E}$ was paired with Cx34.7$_{E214K, E223K, E225K}$ for heterotypic FETCH analysis, the two mutant proteins did not dock (FETCH=1.2±0.3; T_{96}=0.37; P=0.64), despite our model predicting strong

interaction. Follow-up confocal imaging analysis of HEK 293FT cells expressing the constructs revealed that Cx34.7$_{E214K, E223K, E225K}$ failed to properly localize to the cell membrane (compare Fig. 4D and 4E). We did not test this failed mutant this against Cx36 or Cx43; rather, we evaluated an intermediate Cx34.7 mutant protein that maintained positively charged residues at three of the four critical interacting positions, Cx34.7$_{E214K/E223K}$. This mutant showed strong attractive interactions with Cx35$_{K221E}$ in our computational model, and it localized to the cell membrane where it docked with Cx35$_{K221E}$ as confirmed via FETCH analysis and confocal microscopy (FETCH=35.7±4.1%; T_{96}=-28.11; P=2.0×10^{-48}; see Fig. 4F). Critically, Cx34.7$_{E214K/E223K}$ did not show homotypic docking in our FETCH analysis (FETCH=1.1±0.2%, T_{96}=0.46, P=0.68), nor did it dock with Cx36 or Cx43 (FETCH=1.0±0.2, T_{96}=0.58, P=0.72 and FETCH=0.9±0.1%, T_{96}=0.73, P=0.77 for Cx34.7$_{E214K/E223K}$/Cx36 and Cx34.7$_{E214K/E223K}$/Cx43, respectively). From here on, we refer to this rationally designed, exclusively heterotypic and mammalian CNS orthogonal connexin pair, Cx34.7$_{E214K/E223K}$ and Cx35$_{K221E}$, as Cx34.7$_{M1}$/Cx35$_{M1}$ (designer Cxs version 1.0, from *Morone americana*).

Synthetic Cx34.7$_{M1}$/Cx35$_{M1}$ electrical synapses regulate behavior

Using our novel designer Cxs, we set out to determine whether Cx34.7$_{M1}$/Cx35$_{M1}$ could establish functional gap junctions with electrical properties sufficient to synchronize the activity of distinct neurons that compose a circuit. We capitalized on *C. elegans* for this analysis because the nematode nervous system is composed of well-characterized circuits of individual cells that regulate behavior.

C. elegans do not have an innate temperature preference and can thrive in a broad range of temperatures [21]. However, *C. elegans* trained at a particular temperature in the presence of food will migrate towards that temperature when they are subsequently placed on a temperature gradient without food [21]. This learned behavioral preference is in part mediated by plasticity of the chemical synapse occurring between a thermosensory neuron (called AFD, presynaptic) and an interneuron

(called AIY, postsynaptic) [22]. Critically, plasticity in the thermosensory neuron AFD can be genetically manipulated to affect transmission to AIY, and to predictably code the otherwise learned behavioral preference [23].

As with other invertebrates, *C. elegans* do not express connexins. Thus, ectopic expression of vertebrate connexins result in the formation of electrical synapses that are inert to endogenous gap junction proteins. We have previously shown that ectopic expression of Cx36 could be used to edit the thermotaxis circuit, by bypassing the presynaptic plasticity mechanisms between thermosensory neuron AFD and interneuron AIY that contribute to the learned temperature preference [23]. As such, these circuit-edited animals show a persistent preference for warmer temperatures (Fig 5A). We therefore used the thermotaxis circuit in *C. elegans* to validate *in vivo* the utility of our engineered gap junction proteins via *de novo* formation of electrical synapses (assessed by calcium imaging) and to recode behavior (assessed by quantitative thermotaxis behavior testing).

We first expressed $Cx34.7_{M1}/Cx35_{M1}$ cell-specifically in the AFD/AIY pair and examined whether these proteins were capable of reconstituting functional electrical synapses (see supplemental fig. S1 and supplemental table S2). Like Cx36/Cx36, expression of $Cx34.7_{M1}/Cx35_{M1}$ between the AFD/AIY pair resulted in functional coupling between AFD and AIY, as assessed via calcium imaging (Fig. 5B left and 5C; $P<0.0005$ using Fisher exact test with an FDR correction). These *C. elegans* constitutively migrated towards warmer temperatures when placed on a thermal gradient, again mirroring the animals expressing ectopic Cx36/Cx36 ($F_{7,17.91}= 84.99$; $P<0.0001$ using Welch one-way ANOVA followed by Dunnett's T3 multiple comparisons; $p<0.005$; Fig. 5B right and 5D). Expression of $Cx34.7_{M1}$ or $Cx35_{M1}$ in both the AFD and AIY neurons (i.e., $Cx34.7_{M1}/Cx34.7_{M1}$ or $Cx35_{M1}/Cx35_{M1}$) failed to reconstitute an electrical synapse, though homotypic configuration of both wild type connexins (i.e., $Cx34.7_{WT}/Cx34.7_{WT}$ and $Cx35_{WT}/Cx35_{WT}$) synchronized the two cells and modulated behavior (Fig 5B-D; $P<0.0005$). Taken together, these findings confirmed that our designer heterotypic gap junction, $Cx34.7_{M1}/Cx35_{M1}$, exhibit

electrical properties sufficient to synchronize the activity of specific neurons *in vivo*, and rationally recode the behavior. Moreover, our findings confirmed the docking properties we predicted for a range of connexin proteins using our *in vitro* screen and *in silico* studies, since both Cx34.7$_{M1}$ and Cx35$_{M1}$ failed to exhibit homotypic docking.

Synthetic Cx34.7$_{M1}$/Cx35$_{M1}$ electrical synapse enhances synchrony within a mammalian neural circuit

Having established the docking selectivity and *in vivo* functionality of our Cx34.7$_{M1}$/Cx35$_{M1}$ pair, we set out to determine whether the synthetic electrical synapse that they form can be used to modulate neural circuitry in a species with endogenous connexins. Thus, we chose to edit a neurocircuit in the mammalian brain composed of two distinct cell types. We used mice to achieve cell type specificity, because they are highly amenable to cell-type specific access via selective promoters and Cre-recombinase targeting. Excitatory pyramidal neurons (PYR) and parvalbumin expressing fast-spiking interneurons (PV+) can form microcircuits whereby PYR neurons excite PV+ neurons, which in turn inhibit PYR neurons (Fig. 6A, top). This PYR↔PV+ neural circuit has been well characterized in the hippocampus, where PYR neurons show activity coupled to the phase of theta frequency (4-10Hz) oscillations during spatial exploration [24] and PV+ neuron activity correlates with gamma frequency oscillations (30-80Hz)[25]. Critically, the activity of this PYR↔PV+ microcircuit is reflected in the millisecond resolved synchrony between the phase of theta oscillations and the amplitude of gamma oscillations in rodents [26].

PYR↔PV+ microcircuits are also observed in the prefrontal cortex with slightly different neurophysiological properties [27]. Like the cellular dynamics observed in the hippocampus, prefrontal cortex PYR neurons phase couple to locally recorded theta oscillations[28]. On the other hand, in prefrontal cortex, PV+ neurons best couple to the phase and amplitude of local high frequency oscillations (80-200Hz)[29]. Thus, to determine the effect of our synthetic synapses, we quantified the

coupling between the phase of prefrontal cortex theta oscillations and the amplitude of prefrontal cortex high frequency oscillations as a proxy for prefrontal cortex PRY ↔ PV+ microcircuit activity. We then expressed our synthetic $Cx34.7_{M1}/Cx35_{M1}$ synapse at the PRY→PV+ interface, hypothesizing that this manipulation would enhance the millisecond-timed coupling between theta and high frequency oscillations in the prefrontal cortex.

Specifically, we developed an adeno-associated virus (AAV9-CaMKII-$Cx34.7_{M1}$-mEmerald) to target $Cx34.7_{M1}$ to PYR neurons, and another virus (AAV9-Ef1α-DIO-$Cx35_{M1}$-mApple) to target $Cx35_{M1}$ to cells expressing Cre-recombinase. We then co-injected PV-Cre mice with both viruses bilaterally in the prelimbic cortex (PrL, a subdivision of prefrontal cortex in mice) such that $Cx34.7_{M1}$ is expressed in PYR neurons and $Cx35_{M1}$ is expressed in PV+ neurons (i.e., PYR→PV+ modulation given Cx34.7→Cx35 rectification of our hemichannel pair; N=11; Fig. 6A, bottom). A control distribution of non-edited mice consisted of three groups: C57BL/6J mice that had not been injected with virus (N=29), PV-Cre mice co-injected with AAV9-CaMKII-$Cx34.7_{M1}$-mEmerald and AAV9-Ef1α-DIO-$Cx34.7_{M1}$-mEmerald (which expressed $Cx34.7_{M1}$ in the homotypic non-docking configuration; N=7), and PV-Cre mice co-injected with AAV9-CaMKII-$Cx35_{M1}$-mApple and AAV9-Ef1α-DIO-$Cx35_{M1}$-mApple (to express $Cx35_{M1}$ in the homotypic non-docking configuration; N=7). All mice were subsequently implanted with microwire electrodes bilaterally in prelimbic cortex (see Supplemental Figure S4A). Neural oscillation activity was recorded while mice explored an open field.

To determine the coupling between theta (4-10Hz) and high frequency oscillations (80-200Hz), we isolated local field potential activity in these two frequency bands (Fig 6B). We then determined their phase–amplitude relationships using the established modulation index (z-score), which quantifies the statistical likelihood that measured relationships between two oscillations would be observed by chance [30]. Using this approach, we found significant theta–high frequency oscillation coupling from at least one recording site in 85% (46/54) of the implanted mice (Fig. 6C). Moreover, theta–high frequency

oscillation coupling was significantly higher in the mice expressing our synthetic synapse, compared to the pooled group of non-edited control mice (U=1045; P<0.002 using one-tailed rank-sum test). Thus, we found that expression of the synthetic synapse was sufficient to enhance millisecond-timed synchrony within a circuit defined by two precise cell types in mammals. Interestingly, our post-hoc analysis also found no differences in theta–high frequency coupling between mice expressing $Cx34.7_{M1}/Cx34.7_{M1}$ or $Cx35_{M1}/Cx35_{M1}$ in the homotypic non-docking configuration compared to uninjected C57BL/6J control mice (U=509 and 542; P=0.28 and 0.84 using two tailed rank-sum test, for $Cx34.7_{M1}/Cx34.7_{M1}$ or $Cx35_{M1}/Cx35_{M1}$, respectively). These findings from our homotypic controls confirm the non-homotypic docking selectivity of the two mutant proteins.

Synthetic $Cx34.7_{M1}/Cx35_{M1}$ electrical synapse modifies stress behavior in mammals

Finally, we set out to determine whether our synthetic synapse could be used to edit the function of a long-range circuit and modify behavior. The Infralimbic cortex (IL, another anatomical subdivision of medial prefrontal cortex in mice) sends a monosynaptic projection to medial dorsal thalamus (MD) in mice. To target this circuit, we injected BALB/cJ mice with AAV9-CaMKII-$Cx34.7_{M1}$-mEmerald bilaterally in IL. Three weeks later, we injected them with AAV9-CaMKII-$Cx35_{M1}$-mApple bilaterally in MD (i.e., IL→MD modulation, given Cx34.7→Cx35 rectification of the hemichannel pair; Fig. 6D; N=10 mice; see Supplemental Figure S4B). A negative control group of mice was injected with either AAV9-CaMKII-$Cx34.7_{M1}$-mEmerald (N=8) or AAV9-CaMKII-$Cx35_{M1}$-mApple (N=8) in both regions to express synthetic hemichannels across the IL→MD circuit in homotypic non-docking configurations. All mice were subsequently subjected to testing in an open field, immediately followed by a tail suspension test (Fig. 6E).

The tail suspension test is a classic assay that measures the behavioral response of mice to an inescapable negative experience in which they are suspended upside down by their tail [31]. Prior

exposure to stress diminishes behavioral responses during the assay [32], and the assay itself induces a robust stress response [33]. We previously exploited these two features of the test to demonstrate that repeated exposure to the tail suspension test increases immobility during subsequent testing. This stress-induced behavioral adaptation is correlated with functional changes in infralimbic cortex and medial dorsal thalamus. Furthermore, exogenous optogenetic stimulation of the IL→MD circuit, in a manner that recapitulates the normal synchrony in the circuit, reduces behavioral adaptation to acute stress[6]. Critically, no increases in immobility are observed when exploratory behavior is assayed immediately prior to the tail suspension sessions; demonstrating that the behavioral adaptation is specific to the stressful context[6].

Here, we employed this behavioral assay to test whether expression of the synthetic $Cx34.7_{M1}/Cx35_{M1}$ electrical synapses could alter the stress adaptation. Our hypothesis was that the synthetic synapse would synchronize activity between the IL and MD neurons and prevent the immobility adaptation seen on day 2 of the TST. As hypothesized, mice expressing the synthetic synapse across the IL-MD circuit did not show behavioral adaptation in response to repeat tail suspension testing ($F_{1,24}$=7.85, P=0.01 for Group × Day interaction effect using mixed effects model ANOVA; t_9=0.19; P=0.85 for post-hoc testing using two-tailed paired t-test for $Cx34.7_{M1}/Cx35_{M1}$ mice across days; Fig. 6F). On the other hand, increases in immobility were observed in the negative control group (t_{18}=4.9; P=1.7×10^{-4} for post-hoc testing using two-tailed paired t-test for pooled group of $Cx34.7_{M1}/Cx34.7_{M1}$ and $Cx35_{M1}/Cx35_{M1}$ mice across days). As anticipated, post-hoc analysis revealed increases in immobility in both the $Cx34.7_{M1}/Cx34.7_{M1}$ and $Cx35_{M1}/Cx35_{M1}$ groups expressing synthetic hemichannels in non-docking configurations, independently (t_7=3.3; P=0.01, and t_7=5.5; P=9.5×10^{-4}, respectively using two-tailed paired t-test). Thus, expression of our functional synthetic synapse across the IL→MD circuit prevented behavioral adaptation to the tail suspension test. No differences in open field exploration were observed across groups between the mice that expressed $Cx34.7_{M1}/Cx35_{M1}$ and control mice expressing

the hemichannels in non-docking configurations ($F_{1,24}$=0.19, P=0.67 for Group effect; $F_{1,24}$=3.4, P=0.08 for Group × Day interaction effect using mixed effects model ANOVA), demonstrating that editing IL→MD only changed behavior in the stressful assay (Fig. 6F). Both groups of mice displayed higher exploration in the open field during the second testing session ($F_{1,24}$=7.69, P=0.01 for Day effect using mixed effects model ANOVA), demonstrating that the increased immobility displayed by control animals on day 2 of the tail suspension assay was specific to the stress context and not a change in general locomotor activity.

Discussion

We developed a novel approach we term 'Long-term integration of Circuits using Connexins' (LinCx) that can be used to rationally edit brain circuits. This approach employs an engineered connexin hemichannel pair capable of heterotypic, but not homotypic, docking. When expressed in two connected cells, these hemichannels compose a heterotypic electrical synapse, facilitating the transfer of activity between them. We chose to engineer LinCx using two connexin proteins found in *Morone americana* (white perch fish): connexin34.7 (Cx34.7) and connexin35 (Cx35). These connexins are expressed in the CNS at pre-and post-synaptic terminals in *Morone americana* and show rectification in the Cx34.7 to Cx35 direction [12]. Our approach is analogous to the strategy we previously deployed in *C elegans* using Cx36 [23]; however, here our engineered proteins have a preferential direction for facilitating the transfer of electrical activity, and they do not dock homotypically. This latter feature ensures that even when a hemichannel is expressed across a cell type, those cells will not form electrical synapses between themselves (Fig. 1A). Thus, our LinCx system can be deployed in higher order animals, which have many more cells of each given cell type, to target distinct neural circuits. We demonstrated this novel feature in mice by editing a cortical microcircuit composed of two genetically defined cell types.

In order to facilitate such strong docking specificity, we employed a two-part strategy to engineer a Cx34.7 and Cx35 pair that solely exhibit heterotypic docking. First, we created a library of Cx34.7 and Cx35 mutants based on sites previously shown to conferring docking specificity, as well as those implicated in docking based on homology modeling from the structures of Cx26 [34, 35]. We then subjected these mutants to our novel rapid screening approach to identify the mutations that disrupted homotypic docking for each Cx protein. Next, we combinatorially screened non-homotypic Cx34.7 and Cx35 mutant proteins against each other to identify pairs which retained their heterotypic docking character. Second, we developed a computational modeling pipeline to predict and simulate Cx hemichannel docking. We then employed this computational pipeline to probe the docking properties of the mutant proteins identified in our initial FETCH screen and to design new Cx mutants, *in silico.* At each step of our *in silico* design process, we validated the homotypic and heterotypic docking properties of our designed mutants by directly assaying them using our *in vitro* docking screen. Finally, we integrated all the mechanistic understanding of Cx docking interactions gained through this two-pronged approach to engineer Cx34.7 and Cx35 mutants that show heterotypic, but not homotypic, docking. To our knowledge, this exclusively heterotypic docking profile has never been observed for pairs of connexin hemichannels. The functionality of our Cx34.7 and Cx35 mutant pair and their unique docking configuration was validated *in vivo*, in *C. elegans,* where we demonstrated that their expression in two distinct cells can edit the circuit between them and modulate behavior.

We also optimized the translational potential for LinCx by engineering Cx34.7 and Cx35 to not only disrupt their homotypic docking, but also to disrupt their heterotypic hemichannel docking with other connexin proteins endogenous to the human brain (e.g., Cx36, Cx43, and Cx45). Given the sequence homology/identity of ELs across mammals (see supplemental Figure S2), we believed that our tool can be broadly applicable to other preclinical model organisms including rodents and non-human primates. To demonstrate this wide applicability, we validated this unique feature of LinCx directly in mice, where

we found that LinCx successfully edited dynamics that putatively reflect a microcircuit composed of two genetically distinct cell types.

Within brain circuits, space is operationalized as the physical boundaries of individual cells, and time is operationalized as the sub-millisecond level electrical changes of those cells. Though many classic electrical stimulation approaches exhibit high temporal precision in their targeting, these techniques often stimulate volumes of brain tissue that include many brain cell-types and local axonal fibers of passage (see Supplemental Fig. S5; electrical stimulation). Preclinical approaches such as optogenetics provide a substantial improvement with regard to spatial targeting by enabling the selective stimulation of specific cell bodies (based on their genetic identities). Moreover, optogenetics modulates cells via temporally precise light pulses, maintaining the temporal precision of electrical stimulation. Nevertheless, both electrical and optogenetic stimulation bear substantial potential to override circuit computations, which integrate space and time across precise cell types, since these approaches are typically utilized under conditions that modulate the activity of many neurons concurrently and outside of the activity context of their inputs (see Supplemental Fig. S5; optogenetics -soma stimulation).

Over the last decade, several strategies have been employed across myriad studies to enhance the context precision of circuit targeting. One such strategy is based on selectively modulating projection neurons, whereby the inputs at a targeted brain site are selectively activated (Supplemental Fig. S5; optogenetics -projection stimulation) [36]. By directly modulating presynaptic nerve fibers, investigators can regulate the context (presynaptic neurotransmitter release) that drives the target cellular response. Nevertheless, this approach has the potential to change physiological variables that define the context of the presynaptic neuron (and thus the circuit). For example, terminal stimulation can activate axonal collaterals of the presynaptic neuron thereby decreasing the spatial precision of circuit targeting, or it can induce retrograde activation of the presynaptic cell in a manner that disrupts the activation context

of that neuron relative to its own inputs. This approach can also drive the activation of non-target circuits since inputs from a brain region can synapse onto multiple distinct cell types.

Other strategies utilized to enhance the context precision of circuit targeting include the stable step function opsins (SSFOs) [37] and designer receptors exclusively activated by designed drugs (DREADDs) [38], which function to increase the resting membrane potential of target cells. SSFOs and DREADDs maintain the cell type specific spatial precision characteristic of initial optogenetic targeting approaches. Moreover, because cells are rendered more likely to fire in response to their input signals under optimal conditions, these approaches provide improved temporal and context precision. Nevertheless, SSFOs and DREADDs can render target neurons more responsive to all their excitatory inputs (including those from non-targeted circuits), raising the potential of circuit-level off-target effects (see Supplemental Fig. S5; DREADDs). Thus, there is still demand for neuromodulation approaches that function within the spatial, temporal, and context constraints that together define brain circuit operation.

Another strategy to address limitations in context precision is to deliver stimulation within a closed loop framework. In this framework, neural activity is modulated based the ongoing activity in the brain. For example, stimulating hippocampus at the peak vs. trough of the endogenous theta oscillatory cycle differentially impacts spatial memory [39]. In our prior work exploring the circuitry underlying stress-induced behavioral adaptation, we stimulated neurons in medial dorsal thalamus while mice were engaged in a tail suspension test [6]. When we activated neurons based on ongoing oscillatory activity in infralimbic cortex during the test (i.e., closed loop circuit stimulation), mice showed decreased immobility. Conversely, when we stimulated these same cells using two distinct temporal patterns that were untimed to activity in infralimbic cortex, we observed either increased behavioral immobility, or no behavioral effect at all. Additionally, no behavioral effect was observed when we stimulated the terminals of infralimbic cortex neurons in medial dorsal thalamus. Together, these observations provided evidence that context precision serves as another critical axis of circuit operation in the brain

that is orthogonal to both spatial and temporal precision. Moreover, these findings highlighted an ideal circuit and behavioral paradigm to test our new neuromodulation approach that was designed to preserve the spatial, temporal, and context precision of neural circuits.

Here, we found that LinCx modulation of the IL→ MD circuit decreased immobility during repeated tail suspension testing: a behavioral outcome that we could only previously achieve through closed loop stimulation. Interestingly, mice expressing LinCx exhibited normal behavior on the first day of tail suspension testing (t_{24}=1.57; P=0.13 compared to non-edited mice using post-hoc testing with unpaired two-tailed t-test). This suggests that rather than suppressing acute stress behavior per se', LinCx actually enhances the compensatory function of endogenous IL→MD circuitry, ultimately suppressing behavioral adaptation in response to acute stress. As such, our findings suggest that LinCx likely enhances circuits within their physiological range, rather than driving them into supraphysiological states. This observation is supported by our prelimbic cortex micro-circuit editing findings which revealed that the majority of LinCx edited mice exhibited cross-frequency coupling that was less than the upper bound of the non-edited mice. Nevertheless, further testing is necessary to confirm this feature of LinCx.

Like established protein-based modulation tools such as optogenetics and DREADDs, LinCx can be targeted to precise cell types. However, LinCx builds upon these technologies by enabling each hemichannel to be expressed in a different cell type. The hemichannels expressed by these two distinct cell types then integrate *in vivo* to form an electrical synapse. As such, LinCx offers unprecedented spatial precision compared to optogenetics and DREADDs in that it enables targeting of one of the specific spatial features that constrains circuits (e.g., the structural integration of two distinct cell types). Importantly, no electrical synapses are constituted between distinct cells of the same cell type since we disrupted both hemichannels' abilities to dock homotypically (Fig. 1A). LinCx is also designed to optimize the context precision of neuromodulation. Because this electrical synapse rectifies and it only forms between the target pre- and post-synaptic neuron, LinCx constrains the modulation of each individual

post-synaptic neuron by the endogenous activity of its genetically defined pre-synaptic partner. This feature yields a level of temporal precision that mirrors the precision of endogenous brain activity, as confirmed by the enhanced millisecond-precision coupling of local neural activity to the phase of theta oscillations (i.e., periodicity of 100-250ms) observed in our LinCx edited mice. Critically, this feature also suggests that LinCx only potentiates circuit activity within the broader brain state context for which those circuits are typically engaged (i.e., the presynaptic neuron remains under the normal control of its own inputs). Finally, unlike established modulation approaches, LinCx does not require an exogenous actuator such as light, electricity, or an inert pharmacological compound. Rather, LinCx utilizes endogenous brain activity to modulate target neurons, yielding a tool for precise circuit editing.

The integrated engineering approach we utilized to develop LinCx (see Fig. 2) can likely be deployed to develop a toolbox of connexin protein pairs that exhibit selective docking properties. Future work may also yield novel hemichannel pairs with customized conductance properties, mirroring approaches applied to modify the conductance of invertebrate electrical synapses [40]. Thus, we believe that it may be possible to deploy multiple LinCx pairs in the same animal to simultaneously edit multiple circuits and ultimately regulate brain function. Critically, LinCx can also be deployed alongside other well established preclinical modulation approaches including optogenetics and DREADDs, enabling broad manipulation of brain networks across multiple scales of spatial, temporal, and context resolution concurrently.

Direct stimulation of the brain is a well-established treatment for neurological and psychiatric disorders. For example, electrical convulsive therapy (ECT), which delivers energy to the whole brain, has remained the most effective treatment for major depressive disorder for nearly a century [41]. Deep brain stimulation (DBS) of the sub thalamic nucleus is a widely utilized therapeutic for Parkinson's disease [42]. Nevertheless, both these modalities have important spatiotemporal constraints. ECT can induce short term cognitive dysfunction, likely due to the spatially untargeted nature of energy delivery to the brain, ultimately limiting its clinical use. On the other hand, DBS of the subthalamic nucleus has limited

impact on the devastating emotional and cognitive symptoms that accompany Parkinson's disease, likely due to the brain region targeting selectivity [42]. While non-invasive techniques such as transcranial magnetic and focused ultrasound hold future promise for expanding the therapeutic landscape for brain disorders due to their increased clinical accessibility (these approaches do not require anesthesia/brain surgery), there continues to be demand for novel therapeutic approaches that modulate brain activity within both the spatial and temporal constrains of brain circuit activity.

We believe there is great potential for LinCx as a tool to probe the causal relationship between brain circuit function and behavior, and as a potential therapeutic approach to ameliorate human neuropsychiatric disorders. Moreover, there are many potential applications for LinCx technology that extend beyond the central nervous system. For example, future studies could optimize and deploy LinCx to the neuromuscular junction as a potentially treatment for Myasthenia Gravis, the cardiac nervous system as a potential treatment for arrhythmias, to the splenic nerve to regulate inflammation, the autonomic nervous system as a potential treatment for a range of disorders associated with gastrointestinal dysfunction, or to the integumentary system to ameliorate chronic pain.

Figure Legends

Figure 1: Screening to identify mutant connexin hemichannel pair that exhibits exclusively heterotypic docking. **A)** Schematic outlining the limitation of introducing ectopic wild type connexin hemichannels (pink rectangles) as a method for selectively modulating precise neural circuits composed by brown and light green neurons (left). Note that connexin hemichannels yield off-target electrical synapses between pre-synaptic neurons and, thus, off-target modulation of other circuits. Putative strategy for deploying exclusively heterotypic docking hemichannels (green and red rectangles) to selectively modulate precise neural circuits (right). Note the rectification of this putative gap junction. **B)** Counterpart fluorescently

labeled connexin proteins (i.e., C-terminally fused mEmerald or RFP670) are expressed in different cell populations. Cells are then combined and accessed for opposing hemichannel internalization using flow cytometry (left). Representative flow cytometry plot for wild type Cx34.7/Cx35 pair is shown on top, and representative flow cytometry plot for Cx36/Cx45 pair is shown on bottom (right). Pink square highlights portion of individual cells labeled by two distinct fluorescent proteins. **C)** Schematic of *Morone Americana* Cx34.7 and Cx35 extracellular loop mutations used to screen for novel, heterotypic exclusive hemichannels. Positions and mutations unique to Cx34.7 and Cx35 are shown in green and red, respectively. Positions and mutations common to both proteins are shown in black. **D-E)** Circular plot showing homotypic FETCH results for d) Cx34.7 and e) Cx35 mutations. Bar graphs show the effect size (portion of dual labeled cells) of homotypic mutant combinations relative to the heterotypic pairing of human Cx36 and Cx45 which fails to dock. Mutations that disrupted docking are highlighted by black arrows. Purple circle corresponds to zero effect size. Black line corresponds to scale bar for effect size. **F)** Heterotypic FETCH results for Cx34.7 and Cx35 mutant protein combinations. Bar graphs show the effect size of homotypic mutant combinations relative to the wild type Cx34.7 and Cx35 pair.

Figure 2: Integrated approach used to model connexin hemichannel docking. Our approach consists of seven integrated components: 1) homology model generation, 2) *in silico* protein mutagenesis, 3) embedding of proteins in a lipid bilayer and aqueous solution, 4) system minimization, equilibration, and molecular dynamics simulation, 5) residue-wise energy calculation, 6) *in vitro* protein mutagenesis, and 7) FETCH validation.

Figure 3: Model of extracellular loop -2 (EL2) residues mediating homotypic and heterotypic hemichannel connexin docking. A-C) EL2-to-EL2 interactions predicted between wild type Cx34.7 and Cx35 using homology modeling. Residues predicted to form strong attractive/repulsive interactions are highlighted in blue/red respectively (top). Contact plots for EL2-to-EL2 interactions produced by molecular dynamics simulation (middle), and summary of interactions predicted to stabilize

hemichannels pairs (bottom). Plots are shown for A) homotypic Cx34.7, B) homotypic Cx35, and C) heterotypic Cx34.7 and Cx35 interactions.

Figure 4: Engineering Cx34.7 and Cx35 mutants to show heterotypic, but not homotypic, hemichannel docking. A-C) Homology models predicting EL2-to-EL2 residue interactions for Cx34.7 and Cx35 mutant hemichannels. Residues predicted to form strong attractive/repulsive interactions are highlighted in blue/red respectively (top). Contact plots for EL2-to-EL2 interactions produced by molecular dynamics simulation (middle), and summary of interactions predicted to stabilize/destabilize hemichannels pairs (bottom). Plots are shown for A) homotypic $Cx34.7_{E214K, E223K}$, B) homotypic $Cx35_{K221E}$, and C) heterotypic $Cx34.7_{E214K, E223K}$ and $Cx35_{K221E}$ interactions (Cx34.7 residues are shown along the y-axis and Cx35 residues are shown along the x axis). **D-F)** Confocal images of heterotypic connexin pairs D) $Cx34.7_{WT}/Cx35_{WT}$, E) $Cx34.7_{E214K, E223K, E225K}/Cx35_{K221E}$, and F) $Cx34.7_{E214K, E223K}/Cx35_{K221E}$ expressed in HEK 293FT cells. All Cx34.7 and Cx35 proteins are expressed as mEmerald and RFP670 fusion proteins, respectively. White arrows highlight dual fluorescent labeled vesicles. Note the cytoplasmic localization of $Cx34.7_{E214K, E223K, E225K}$ in panel E.

Figure 5. Ectopic connexin hemichannels couple *C. elegans* neurons and recode thermal preference. A) Schematic of the AFD→AIY synaptic communication and expressed temperature preference. The AFD thermosensory neuron has a robust calcium response to warming stimuli. *C. elegans* raised in the presence of food at 15°C, or animals with a Protein Kinase C (PKC)-*1* gain-of-function mutation, move towards cooler temperatures when placed on a thermal gradient (top). Ectopic expression of connexin hemichannels between AFD and AIY results in synchronization of the signal to AIY and promotes warm-seeking behavior (bottom). **B)** Calcium traces of neurons expressing ectopic connexin hemichannel pairs (left). Baseline AFD and AIY responses are also shown. Each panel depicts the average trace a group (top, data shown as mean±SEM), heatmaps of individual animals (middle), and the temperature stimulus (bottom). Behavioral traces for each group are shown on the right. Traces are shown for C. *elegans*

homotypically expressing wild type connexin hemichannels (pink highlight), heterotypically expressing the mutant pair (tan highlight), and homotypically expressing mutant connexin hemichannels (cyan highlight). **C)** Portion of animals showing neuronal calcium responses based on the traces shown in B; ***p<0.0005 using Fisher's exact test for penetrance. Error bars denote 95% C.I. **D)** Thermotaxis indices corresponding to experimental groups. Each data point represents the thermotaxis preference index of a separate assay (12-15 animals/assay), with the median for each group plotted denoted by a black horizontal. **p<0.005; ***p<0.0005; Error bars denote 95% C.I.

Figure 6. LinCx edits microcircuit relevant dynamics in mice. A) Prefrontal cortex microcircuit comprising an excitatory pyramidal neuron (PYR) and a parvalbumin expressing fast-spiking interneuron (PV+). The tan circle highlights the target for synaptic editing (top). PV-Cre mice were bilaterally co-injected with AAV-CaMKII-Cx34.7$_{M1}$ and AAV-DIO-Cx35$_{M1}$ (bottom). Control mice were injected with a Cx34.7$_{M1}$ or Cx35$_{M1}$ pair of viruses which expressed the same hemichannel in both cell types. Mice were subsequently implanted with microwires in prefrontal cortex. **B)** Representative local field potential recorded from prefrontal cortex (top). Power spectrograms show theta (4-10Hz) and high frequency activity (80-200Hz), which corresponds to PYR and PV+ neuron firing, respectively (middle). Microcircuit function is represented by the coupling between the phase of theta oscillations (black) and the amplitude of high frequency oscillations (red, bottom). **C)** Distribution of theta–high frequency coupling scores observed across un-injected C57BL/6j mice (N=29, black), PV-Cre mice co-injected with a Cx34.7$_{M1}$ (N=7) or Cx35$_{M1}$ (N=5) pair of viruses (blue), or mice co-injected with a docking Cx34.7$_{M1}$/Cx35 $_{M1}$ pair (N=12, tan). Mice co-injected with the Cx34.7$_{M1}$/Cx35 $_{M1}$ pair showed significantly higher theta-high frequency oscillation coupling than non-edited mice (U=953; P=0.0036 using one tailed rank-sum test). D) Schematic of Infralimbic cortex → Medial dorsal thalamus circuit targeted for editing, and viral injection strategy. **E)** Schematic of behavioral testing to quantify stress induced behavioral adaptation. **F)** Immobility time and distance travelled during repeat tail suspension (left) and open field testing (right).

Mice co-injected with $Cx34.7_{M1}$ (N=8) or $Cx35_{M1}$ (N=8) in homotypic non-docking configurations showed stress-induced behavioral adaptation during repeat TST testing (blue), while mice co-injected with the functional $Cx34.7_{M1}$/$Cx35_{M1}$ pair did not (N=10; tan). No significant behavioral differences were observed between viral groups in the open field; ^ denotes Group effect; # denotes Group × Day interaction effect using mixed effects model ANOVA.

Materials and Methods

Design of Cx34.7 and Cx35 mutant library

A semi-rational design approach was used to design the mutant library. Sequence alignments between the *Morone americana* connexins and the connexins for which the most structure-function data existed (Cx26, Cx32, Cx36, Cx40, and Cx43) were performed in ClustalW. Sites identified by previous studies as conferring specificity for docking were used as well as those identified by homology modeling from the structures of Cx26 [11]. Specifically, we primarily focused on the extracellular loops and four residues at the interface in loop two, KEVE/KDVE (*M. americana* Cx34.7/Cx35) and one residue of E1. The homologous residues in other connexins had been demonstrated to be highly tolerant to mutation and critical for docking specificity [43]. Mutations were modeled in Swiss PDB Viewer using homology models of Cx34.7 and Cx35 from a Cx26 and Cx32 interface structure so as not to create mutations with obvious steric hindrance. A wide range of substitutions was made for these five residues of interest, including both those intended to introduce compatible electrostatic interactions as well as less likely candidates. Mutations were also created targeting other residues nearby and/or adjacent to these five for which there was some evidence in the literature that they contributed to docking specificity. However, our semi-rational approach was such that not as many variants were tried for these more

distal site mutations and the mutations that were made in those sites were more conservative with regard to the steric and electrostatic properties of the change.

Construct cloning and preparation

Morone Americana Cx34.7 and Cx35 cDNA constructs we initially acquired failed to efficiently express in in HEK 293FT cells. Thus, Connexin gene information was procured from the National Center for Biotechnology Information (NCBI, ncbi.nlm.nih.gov) and the Ensembl genome browser (ensembl.org). The human codon-optimized genes were ordered from Integrated DNA Technology as gBlocks Gene Fragments (IDT, idtdna.com). To generate constructs for transient transfection of HEK 293 FT cells, genes were subcloned into Emerald-N1 (addgene:53976) and piRFP670-N1 (addgene: 45457) vectors using In-Fusion cloning (takarabio.com), resulting in connexin fluorescent fusion proteins, specifically with the fluorescent proteins being adjoined to the connexin carboxy-terminus. Mutant constructs were generated by employing overlapping primers within standard Phusion polymerase PCR reactions to facilitate site-directed mutagenesis.

The Gateway recombination (Invitrogen) system was used to generate all Connexin 36, Cx34.7, Cx35, wild type and mutant protein *C. elegans* expression plasmids. For PCR-based cloning and subcloning of components into the Gateway system, either Phusion or Q5 High-Fidelity DNA-polymerase (NEB) was used for amplification. All components were sequenced within the respective Gateway entry vector prior to combining components into expression plasmids via a four-component Gateway system [44]. The different connexins versions were introduced into pDONR221a using a similar PCR-based strategy from plasmid sources [45-47]. Cell-specific promoters were introduced using the pENTR 50 -TOPO vector (Invitrogen) after amplification from genomic DNA or precursor plasmids. Transgenic lines were created

by microinjection into the distal gonad syncytium [48] and selected based on expression of one or more co-injection markers: Punc-122::GFP, Pelt-7::mCherry::NLS.

Cell Culture

HEK 293FT cells were purchased from Thermo Fisher Scientific (cat# R70007) and were maintained according to manufacturer instructions. Briefly, cultures were grown in 10 cm tissue culture treated dishes in high-glucose DMEM (Sigma Aldrich, D5796) supplemented with 6mM L-glutamine, 0.1 mM MEM non-essential amino acids and 1 mM MEM sodium pyruvate in a 5% CO_2, 37°C incubator. Cells were passaged via trypsinization every 2-3 days or until 60-80% confluency was reached.

FETCH data analysis

Complete FETCH methodology is outlined in Ransey et. al. 2021 [15]. Briefly, replica multi-well plates with HEK 293FT cells were transfected with either of the two connexin proteins being evaluated for docking. Following a transfection incubation period, experimental counterparts were combined, replated, and further incubated for ~20-24hrs, allowing cells to make contacts and potentially generate connexosomes. Co-plated samples were trypsinized, fixed in suspension, and analyzed via flow cytometry. Flow cytometry data was processed with two selection gates prior to their fluorescence evaluation. First, putative HEK cells were identified by evaluating sample forward vs. side scatter area. Next, single cells were identified as the putative cells that maintained a linear correlation of forward scatter height to forward scatter area. Finally, the dual fluorescence (mEmerald vs. RFP670) profiles of each sample was generated, and the FETCH score was defined as the proportion of dual-labeled fluorescent cells that develop in a co-plated sample.

For screening analysis, five FETCH replicates were obtained for each condition (mutation). These scores were benchmarked against scores for Cx36 and Cx45 (FETCH=1.2±0.1%, N=54 replicates). To quantitatively determine whether a connexin pair docked, we determined FETCH scores for the dual

fluorescence of cells under conditions where docking was not anticipated. These conditions included pairs of connexins previously established to not show docking: Cx36 and Cx45 (FETCH=0.7±0.0%, N=59 replicates), homotypic Cx23 (FETCH=0.9±0.4%, N=6 previously collected replicates[15]), Cx36 and Cx43 (FETCH=1.2±0.2%, N=10 previously collected replicates[15]), and under conditions for which cells were transfected with cytoplasmic fluorophores rather than tagged connexins (FETCH=4.4±0.6%, N=17 previously collected replicates[15]). These 92 FETCH scores were used as the 'known-negative' distribution. FETCH scores from each experimental condition were then compared against the established negative score distribution using a one-tailed t-test, with a Bonferroni correction for the total number of experimental conditions tested. These FETCH replicates were independent of the replicates utilized for our screening analysis. Stats are reported as mean±s.e.m, and only uncorrected P values are reported through the text.

Confocal Imaging Analysis of Gap Junction Partners

For imaging of putative gap junction partners, different populations of HEK 293FT cells were transfected with counterpart connexin proteins, incubated, and combined as described for FETCH analysis. Combined samples of HEK 293FT cells were co-plated onto 10 ug/ml Fibronectin coated 35 mm, glass-bottom Mattek dishes (cat# P35GC-1.5-14-C). Cells were imaged at ~20 hrs post co-plating. Images were acquired on a Leica SP5 laser point scanning inverted confocal microscope using Argon/2, HeNe 594nm and HeNe633nm lasers, conventional fluorescence filters and a 63X, HCX PL APO W Corr CS, NA: 1.2, Water, DIC, WD: 0.22mm, objective. Images were taken with 1024 x 1024 pixel resolution at 200Hz frame rate.

For assessing Cx34.7M1::Cx35M1 expression *in vivo* in *C. elegans*, we imaged strain DCR8669 *olaEx5214 [Pgcy-8::CX34.7(E214K, E223K)::GFP; Pttx-3::CX35(K221E)::mCherry; Punc-122::GFP]*. L4 animals were mounted in 2% agarose in M9 buffer pads and anaesthetized with 10mM levamisol (Sigma). Confocal

images were acquired with dual Hamamatsu ORCA-FUSIONBT SCMOS cameras on a Nikon Ti2-E Inverted Microscope using a confocal spinning disk CSU-W1 System, 488nm and 561nm laser lines and a CFI SR HP PLAN APO LAMBDA S 100xC SIL objective. Images were captured using the NIS-ELEMENTS software, with 2048px x 2048px, 16-bit depth, 300nm step size, 200ms of exposure time and enough sections to cover the whole worm depth.

Protein modeling pipeline

Our protein modeling pipeline is based on previously published methodology [49] and integrates five components: 1) homology model generation, 2) embedding of proteins in a lipid bilayer and aqueous solution, 3) protein mutagenesis, 4) system minimization, equilibration, and molecular dynamics simulation production run, and 5) residue-wise energy calculation.

Homology Modeling

We initially tested five homology modeling software suites: Robetta, SwissModel, Molecular Operating Environment (MOE; Chemical Computing Group ULC, Montreal, QC, Canada, H3A 2R7, 2021), I-Tasser, Phyre2 [50-58]. A quality assessment suite, — MOLProbity [59-61] revealed that Robetta models outperformed the rest, based on a set of standard metrics (Ramachandran plot outliers, clashscore, poor rotamers, bad bonds/angles, etc).

Since our aim was to model the extracellular loops responsible for connexin hemichannel docking, we picked all the resolved connexin structures that possessed a high degree of extracellular loop homology to our connexins of interest as the inputs for Robetta. The top homolog hits were generally the same for the three Cxs of interest: Connexin-26 Bound to Calcium (5er7.1) [35], Human Connexin-26 (Calcium-free) (5era) [35], Structure of connexin-46 intercellular gap junction channel at 3.4 angstrom resolution by cryoEM (6mhq) [62], Structure of connexin-50 intercellular gap junction channel at 3.4 angstrom resolution by cryoEM (6mhy) [62], Structure of the connexin-26 gap junction channel at 3.5 angstrom

resolution (2zw3) [34]. Cx34.7 and Cx35 wild type sequences had the greatest homology degree with 6mhq, while Cx36 was most homologous to 5er7.1. We generated three wild type hemichannels for Cx34.7, Cx35, and Cx36.

System Assembly

Next, we assembled hemichannels into homotypic and heterotypic gap junctions, embedded them in two double bilayers, dissolved them in water, and added appropriate ion concentrations for the extracellular and two intracellular compartments. The primary software suite used for this modeling step was VMD [63, 64]. We also utilized CHARMM GUI to generate the naturalistic model of a region of a double bilayer [65-69]. Membrane components were then selected in appropriate proportions to resemble experimentally-derived data from a neuronal axonal membrane.

Specifically, since Robetta was unable to model the full gap junction, we merged hemichannels into full homotypic/heterotypic gap junctions in a semi-automated way. First, to make homotypic gap junctions, we loaded the two-homology models for a hemichannel. We then aligned them using the center of mass of the extracellular loops. A slight rotation along the z axis was implemented for several pairs to optimize their fit. To make heterotypic gap junctions, we created a homotypic gap junction for each hemichannel, aligned the extracellular loops for the two homotypic gap junctions, then removed an opposing hemichannel from each homotypic gap junction (leaving the two different hemichannels aligned). Next, using the constructed gap junction, we aligned two pre-made membrane bilayers with the center of mass assigned as each embedded hemichannel. We then removed membrane molecules that overlapped with the hemichannel or the hemichannel pore. Next, we dissolved the system in water, and removed water that overlapped with the lipid bilayer. Extracellular water was then separated to a new file, where Na+, K+, Cl-, and Ca2+ ions were added to yield concentrations mirroring the extracellular environment of mammalian neurons [70]. Finally, Na+, K+, Cl-, and Ca2+ ions were added

to the intracellular space to mirror the intracellular environment of mammalian neurons, and the files containing the embedded Cx hemichannels and extracellular water were merged. Notably, these stages were automated yielding a streamlined progression from a protein-only hemichannel model to a fully embedded gap junction model ready for subsequent simulation and/or mutagenesis.

Mutagenesis

We developed a python command-line tool that utilizes VMD to generate mutation configuration files for subsequent MD simulation. Here, we simply specified the connexin hemichannels of interest and the position at which a specific mutation should be introduced.

System Minimization, Equilibration, and MD Simulation Production Run

Next, we minimized atomic energies, equilibrated the system, and ran the stable system in a production simulation run. Specifically, MD simulation was performed using NAMD *[71]* and was divided into five steps:

1) *Melt lipid tails while keeping remaining atoms fixed (simulate for 0.5 ns)*
2) *Minimize the system, then allow the bilayers and solutions to take natural conformation while keeping gap junction fixed (split in two stages to accommodate reduction in volume of relaxing system; simulate 0.5 ns total)*
3) *Release the gap junction and equilibrate the whole system (simulate 0.5 ns)*
4) *Run minimized and equilibrated system in a production run (simulate 0.5 ns)*

Though MD simulation (step 4) is highly reliant on the input file provided by the *System Assembly* process, these steps render the simulation much more robust to modeling imperfections. For example, the membrane model developed though System Assembly is very rigid and has the potential to behave like a solid rather than like a liquid. Thus, melting the lipid tails encourages the model to embody a

liquid. Similarly, many atoms in the input file may have unnatural initial energies, such that if they are all released at once, they would start moving at high velocities and the simulation would fail. Therefore, bringing the system to a local energy minimum increases stability. Removing constraints on the water and lipids enables them to surround the gap junction in a naturalistic form. Finally, releasing the constraints on the gap junction enables it to take the most energetically stable conformation given the environment.

Energy Calculation

To predict the residues that play a prominent role in docking, we quantified all non-bonding interactions between the two connexin hemichannels at key residues on the extracellular loops. Output from the MD simulation was loaded into the VMD "NAMD Energy" plugin. We then calculated nonbonding energies for all residues on each hemichannel that were within 12 angstroms of at least one residue on the other hemichannel. For each residue pair we then averaged energies across the 250 simulation frames

***C. elegans* strains and genetics**

Nematodes were cultivated at 20°C on nematode growth medium seeded with a lawn of Escherichia coli strain OP50 using standard methods [72]. One-day-old adult hermaphrodites were used for all experiments. The strains used in this study are listed in the Strain Table (supplemental table S2). All thermotaxis behavioral assays, molecular biology, transgenic lines, and calcium imaging were performed following the methods of Hawk et al. 2018 [23], with minor modifications as outlined in the following subsections.

Thermotaxis Behavioral Assay

Animals were reared at 20°C for all experiments with shifts to the 15°C training temperature 4 hours prior to testing. High-throughput behavioral analyses were performed as described [23, 73]. Briefly, synchronized 1-day-old adult populations were washed in M9 buffer [74], then transferred by pipette to

the 20°C isotherm of the behavioral test plate (22cm x 22cm plates with a 18°C to 22°C thermal gradient). Each behavioral test plate was split in half along the temperature gradient using a thin and clear plastic divider. This allowed for wild type controls to be assayed on one half of the arena and connexin-expressing animals on the other half. Migration was monitored for 60 min at 2fps using a MightEx camera (BCE-B050-U). Trajectories were analyzed using an adaptation of the MagatAnalyzer software package as previously described [23, 73, 75].

Calcium Imaging in C elegans

For imaging, worms were mounted on a thin pad of 5% agarose in M9 buffer between two standard microscope coverslips. Worms were immobilized with 7.5mM levamisol (Sigma). All solutions were pre-equilibrated to the holding temperature prior to sample preparation. Prepared coverslip assemblies were placed at TH on the peltier surface of the thermoelectric control system. A thermal probe (SRTD-2, Omega) mounted onto the surface of the peltier was used for feedback control via a commercially available proportional-integral-derivative (PID) controller (FTC200, Accuthermo). Target temperatures were supplied to the PID controller by a custom computer interface written in LabView (National Instruments), which subsequently gated current flow from a 12V power supply to the peltier via an H-bridge amplifier (FTX700D, Accuthermo). Excess heat was removed from the peltier with a water-cooling system. Precise temperature control was initially confirmed with an independent T-type thermal probe (IT-24P, Physitemp) attached to a hand-held thermometer (HH66U, Omega) and routinely compared to incubator temperatures with an infrared temperature probe (Actron). After mounting worms and placing them on the thermal control stage, fluorescence time-lapse imaging was begun immediately prior to implementing the temperature protocol in LabView, and temperature readings were recorded continuously while imaging. Fluorescence time-lapse imaging (250ms exposure) was performed using a Leica DM5500 microscope with a 10X/0.40 HC PL APO air objective and a Hamamatsu ORCA-Flash4.0 LT camera. Image acquisition was performed using MicroManager [76]. Segmentation into regions of

interest and downstream data processing was performed using FIJI [77], and custom scripts written in MATLAB (MathWorks), including alignment of fluorescence intensity values to the temperature stimulus, calcium response detection, and initial figure production. Temperature readings were assigned to image frames in MATLAB based on CPU timestamps on images and temperature readings. Heatmaps were displayed using the MATLAB 'imagesc' function, which scales data to the full color range available. The same scaling was applied to all comparable data within a figure. Unless otherwise specified, the scaling was based upon the highest intensity dataset to minimize saturation. For analyses of AFD calcium signals, we measured an ROI of one AFD soma per animal. For analyses of AIY, we quantified signal intensity in the synaptic Zone 2. AIY is a unipolar neuron with both inputs, including those from AFD, in zone 2 and outputs to postsynaptic partners. We also quantified a reference region outside of AIY.

Responses were scored as the initial rise of the AFD or AIY calcium signal as determined by a blind human observer. Consistent with previous reports [78], we observed clear and qualitatively similar responses to thermal stimuli in the synaptic Zone 2 region. The genetic background for the AFD and AIY calcium imaging lines used in this study (control and experimental) contained olaIs23, a caPKC-1 GOF mutation. This was done to match prior work [23] in which Connexin 36 was demonstrated to evoke AFD-locked responses in AIY compared to caPKC-1 animals without Connexin 36.

Vertebrate Animal Care and Use

Male B6.129P2-*Pvalb*$^{tm1(cre)Arbr}$/J (PV-Cre mice) and female C57BL/6J mice (Stock No: 017320 and 000664, respectively) purchased from Jackson labs were bred to generate the male and female (N=28 total virally injected and implanted mice) PV-Cre heterozygous mice subjected to the prefrontal cortex PYR↔ PV+ editing experiment. Male C57BL/6J mice (N=29) purchased from Jackson were utilized for non-edited controls. Mice were housed three-five/cage on a 12-hour light/dark cycle and maintained in a humidity- and temperature-controlled room with water and food available ad libitum. Neural

recordings were conducted during the dark cycle (Zeitgeber time: 13-19), given prior evidence that electrical synapse conductance can be diminished in the retina via circadian regulation (REF). Inbred BALB/cJ male mice (strain: 000651) purchased from the Jackson Labs were used for infralimbic cortex → medial thalamus circuit editing experiments. We chose this strain and sex of mice to mirror our previous study which optogenetically targeted the infralimbic cortex → medial thalamus circuit [6]. Behavioral experiments were conducted during the dark cycle (Zeitgeber time: 9-11). All vertebrate animal studies were conducted with approved protocols from the Duke University Institutional Animal Care and Use Committees and were in accordance with the NIH guidelines for the Care and Use of Laboratory Animals.

Mouse viral injection surgeries

PV-Cre mice were anesthetized with isoflurane (1%), placed in a stereotaxic device, and injected with a 1:1 solution of AAV9-CaMKII-Cx34.7$_{M1}$-mEmerald (titer: 5.0×10^{12} vg/ml) and AAV9-Ef1α-DIO-Cx35$_{M1}$-mApple (titer: 1.3×10^{13} vg/ml), based on stereotaxic coordinates measured from bregma at the skull to target prelimbic cortex bilaterally (PrL: 2.1mm AP, 0.65mm ML, -1.45mm DV from the dura at a 21° angle for male mice, and PrL: 2.05mm AP, 0.62mm ML, -1.41mm DV from the dura at a 21° angle for female mice). A total of 1µL viral solution was delivered to each hemisphere over 10 minutes using a 5µL Hamilton syringe. Control mice were injected with a 1:1 solution of AAV9-CaMKII-Cx34.7$_{M1}$-mEmerald and AAV9-Ef1α-DIO-Cx34.7$_{M1}$-mApple (titer: 1.1×10^{13} vg/ml) or a 1:1 solution of AAV9-CaMKII-Cx35$_{M1}$-mEmerald (titer: 6.9×10^{12} vg/ml) and AAV9-Ef1α-DIO-Cx35$_{M1}$-mApple. These viruses were created in the Duke Viral Vector Core. Viral injections were performed in male and female mice at age 2.5-5 months, and viral manipulations were balanced across cages and sex.

BALB/cJ mice were anesthetized with isoflurane (1%), placed in a stereotaxic device, and injected with AAV9-CaMKII-Cx34.7$_{M1}$-mEmerald (titer: 5.0×10^{12} vg/ml) based on stereotaxic coordinates

measured from bregma at the skull to target infralimbic cortex bilaterally (IL: 1.7mm AP, 0.72mm ML, -2.03mm DV from the dura at an angle of 10°). A total of 0.5µL viral solution was delivered to each hemisphere over 5 minutes using a 5µL Hamilton syringe which was left in place for an additional 10 minutes prior to removal. Three weeks later (see supplemental Figure S4), mice were injected with AAV9-CaMKII-Cx35$_{M1}$-mApple (titer: 6.9×10^{12} vg/ml) based on stereotaxic coordinates measured from bregma at the skull to target medial dorsal thalamus bilaterally (MD: -1.58mm AP, 0.5mm ML, -2.88mm DV from the dura at an angle of 10°). Control mice were injected with AAV9-CaMKII-Cx34.7$_{M1}$-mEmerald in both IL and MD, or AAV9-CaMKII-Cx35$_{M1}$ in both IL and MD, to express the synthetic hemichannels in non-docking homotypic configurations. Viral injections were performed in male mice at age 3 months.

Electrode Implantation Surgery

Mice were anesthetized with isoflurane (1.0%), placed in a stereotaxic device, and metal ground screws were secured to the cranium. For PV-Cre mice, a total of 8 tungsten microwires were implanted in prelimbic cortex (centered at 1.8mm AP, ±0.25mm ML, -1.75mm DV from the dura for male mice; centered at 1.76mm AP, ±0.25mm ML, -1.71mm DV from the dura for female mice). C57BL/6J control mice were implanted at 2 months. A total of 32 tungsten microwires were arranged in our previously described multi-limbic circuit recording design[79]. Briefly, bundles were implanted to target basolateral and central amygdala (AMY), medial dorsal thalamus (MD), nucleus accumbens core and shell (NAc), VTA, medial prefrontal cortex (mPFC), and VHip were centered based on stereotaxic coordinates measured from bregma (Amy: -1.4mm AP, 2.9 mm ML, -3.85 mm DV from the dura; MD: -1.58mm AP, 0.3 mm ML, -2.88 mm DV from the dura; VTA: -3.5mm AP, ±0.25 mm ML, -4.25 mm DV from the dura; VHip: -3.3mm AP, 3.0mm ML, -3.75mm DV from the dura; mPFC: 1.62mm AP, ±0.25mm ML, 2.25mm DV from the dura; NAc: 1.3mm AP, 2.25mm ML, -4.1 mm DV from the dura, implanted at an angle of 22.1°). We targeted cingulate cortex, prelimbic cortex, infralimbic cortex using the mPFC bundle by building a 0.5mm and 1.1mm DV stagger into our electrode bundle microwires. Animals were implanted bilaterally

in mPFC and VTA. All other bundles were implanted in the left hemisphere. The NAc bundle included a 0.6mm DV stagger such that wires were distributed across NAc core and shell. We targeted BLA and CeA by building a 0.5mm ML stagger and 0.3mm DV stagger into our AMY electrode bundle[79].

Neurophysiological Data acquisition

Neural recordings experiments were performed in PV-Cre mice one week after implantation surgery and blind to viral group. Mice were habituated to the recording room for at least 60 minutes prior to testing. PV-Cre mice were connected to a headstage (Blackrock Microsystems, UT, USA) without anesthesia, and given a single saline injection (10mL/kg mouse, intraperitoneally). Notably, these saline injections were performed to facilitate comparison of acquired neural data with future drug studies. Twenty-five minutes later, mice were placed in a 17.5in × 17.5in × 11.75in (L×W×H) chamber for 60 minutes. Recordings were conducted under low illumination conditions (1-2 lux), and only data from the first 10 minutes of exposure to the open field were used for neurophysiological analysis. For C57BL/6J control mice, experiments were performed at least two weeks following implantation surgery. Mice were habituated to the recording room for at least 60 minutes prior to testing, and headstages were connected without anesthesia. Twenty-six male mice were placed in a 17.5in × 17.5in × 11.75in (L×W×H) chamber for 10 minutes, and three mice were recorded in an 19.5in × 12in (D×H) circular chamber. Six of these mice were injected with (10mL/kg mouse, intraperitoneally) 30 minutes prior to recordings, and all recordings were conducted under an illumination of 125 lux.

Neuronal activity was sampled at 30kHz using the Cerebus acquisition system (Blackrock Microsystems Inc., UT). Local field potentials (LFPs) were bandpass filtered at 0.5–250Hz and stored at 1000Hz. All neurophysiological recordings were referenced to a ground wire connected to both ground screws, and an online noise cancellation algorithm was applied to reduce 60Hz artifact.

Determination of LFP cross frequency phase coupling

Signals recorded from all viable implanted microwires were used for analysis. Local field potentials were filtered using 4th order Butterworth bandpass filters designed to isolate theta (4-10Hz) prefrontal cortex oscillations and high frequency oscillations (80-200Hz). The instantaneous amplitude and phase of the filtered LFPs were then determined using the Hilbert transform, and the Modulation index was calculated for each LFP channel using the MATLAB code provided by Canolty et al [30]. Briefly, a continuous variable z(t) is defined as a function of the instantaneous theta phase and instantaneous gamma amplitude such that $z(t) = A_G(t)*e^{i\phi_{TH}(t)}$, where A_G is the instantaneous gamma oscillatory amplitude, $e^{i\phi_{TH}}$ is a function of the instantaneous theta oscillatory phase. A time lag is then introduced between the instantaneous amplitude and theta phase values such that z_{surr} is parameterized by both time and the offset between the two variables, $z_{surr} = A_{HG}(t+\tau)*e^{i\phi_{TH}(t)}$. The modulus of the first moment of z(t), compared to the distribution of surrogate lengths, provides a measure of coupling strength. The normalized z-scored length, or Modulation index, is then defined as $M_{NORM} = (M_{RAW}-\mu)/\sigma$, where M_{RAW} is the modulus of the first moment of z(t), μ is the mean of the surrogate lengths, and σ is their standard deviation [6, 28, 30]. The modulation index scores were averaged across all implanted channels for each mouse (~7.3 channels for each PV-Cre mouse, and 2 channels implanted bilaterally for each C57BL/BJ control mouse).

Behavioral testing of IL ->MDThal circuit manipulation

All behavioral testing was conducted under low illumination conditions (1-2 lux). Two weeks after the second viral surgery, mice were initially placed in a 17.5in × 17.5in × 11.75in (L×W×H) chamber for five minutes of open field testing. Mice were then suspended 1cm from the tip of their tail for six minutes for the tail suspension assay. Open field and tail suspension behavioral data were acquired during a single testing session, and the behavior testing session was repeated the next day. Testing sessions were video recorded, and open field and tail suspension behavior was analyzed using

Ethovision XT 12 (Noldus, Wageniingen, the Netherlands). Behavioral experiments and subsequent video analyses were performed blind to group.

Immunohistochemistry for mouse studies

Mice were perfused transcardially with ice-cold PBS followed by 4% PFA in PBS (EM Sciences, Hatfield, PA). The brains were harvested and coronally sliced in 1X PBS at 35µm using a vibratome (Vibratome Series 3000 Plus, The Vibratome Company, St. Louis, MO) and mounted onto positively charged slides using a mild acetate buffer (82.4mM Sodium Acetate, 17.6mM acetic acid) or 1X PBS solution. Brain slices were covered with DAPI-Mowiol mounting solution [Glycerol, puriss. p.a., Mowiol 4-88 (Sigma-Aldrich, St. Louis, MO), and 0.2M Tris-Cl pH 8.5, DAPI (Sigma-Aldrich, St. Louis, MO)] and cover slipped prior to imaging. Images were obtained using a Nikon Eclipse fluorescence microscope at 4x magnification with illumination source power and exposure kept consistent between samples.

For the PrL PYR→PV+ study, we only used mice with confirmed bilateral Cx expression for neurophysiological analysis(N=26/29). For the IL→MD study, we used mice that showed bilateral Cx expression in one region, and at least unilateral expression in the other region (N=26/35). We chose this strategy since our prior work indicated that unilateral optogenetic stimulation of the IL→MD circuit was sufficient to alter stress related behavior in the tail suspension assay.

Acknowledgements

The authors would like to acknowledge Dr. Terry Oas, Dr. Mike Tadross, Dr. Nicole Calakos, Dr. Marc Caron, Dr. David Carlson, and Dr. Fan Wang for helpful discussion and/or guidance; Dr. Kayla Lemons and Reagan Portelance for technical assistance; and Dr. John O'Brien for supplying reagents. The authors would like to acknowledge the generous funding that has supported this work: Ernest E. Just Life Science Institute Postdoctoral Research Fellowship; Burroughs Wellcome Fund Postdoctoral Enrichment Program Grant (E.R.); Hartwell Postdoctoral Research Fellowship (E.R.); SOM Core Facility Voucher

Program (E.R. and K.D.); NIH grants R01NS076558 and DP1NS111778 (D.C.R.); HHMI Scholar Award (D.C.R.); NIH grants U01HL134764, R01HL132389, and R01HL126524 (N.B.); Duke University School of Medicine MedX Grant (K.D. and N.B.); Duke University Chancellor's Discovery award (K.D. and N.B.); Duke University School of Medicine Kahn Neurotechnology Grant (E.R., N.B., and K.D.); NIH BRAIN Initiative Grant R21EY029451 (K.D. and N.B.); Hope for Depression Research Grant, and NIH Grants R01MH120158 and R01MH125430 (K.D.). A special thanks to Freeman A. Hrabowski, Robert and Jane Meyerhoff, and the Meyerhoff Scholarship Program.

Author contributions

Conceptualization and Methodology – E.R., K.C., E.W., A.A.P., D.C.R., R.H., and K.D.; Formal Analysis – E.R., K.C., G.E.T., E.W., T.R., K.K.C., D.H., A.A.P., S.M., and D.C.R., K.D.; Investigation – E.R., K.C., G.E.T., E.W., R.B., T.R., E.A., K.K.C.W., D.H., H.S., S.M., R.H., A.A.P.; Resources – E.R., N.B., D.C.R., K.D.; Writing – Original Draft, E.R., K.C., E.W., A.A.P., D.C.R., N.B., K.D. Writing – Review & Editing, E.R., K.C., G.E.T., E.W., T.R., A.A.P., K.K.C.W., D.C.R., S.M., R.H., N.B, K.D. Visualization – E.R., K.C., G.E.T., E.W., T.R., A.A.P., D.C.R., K.D.; Supervision – S.M., D.C.R., N.B. and K.D.; Project Administration and Funding Acquisition – E.R., D.C.R., R.H., N.B., and K.D. See Supplemental materials for detailed author contributions.

Declaration of Interests

The authors declare no competing interests

References

1. Jones, M.W. and M.A. Wilson, *Theta rhythms coordinate hippocampal-prefrontal interactions in a spatial memory task.* PLoS Biol, 2005. **3**(12): p. e402.
2. Seidenbecher, T., et al., *Amygdalar and hippocampal theta rhythm synchronization during fear memory retrieval.* Science, 2003. **301**(5634): p. 846-50.
3. Sigurdsson, T., et al., *Impaired hippocampal-prefrontal synchrony in a genetic mouse model of schizophrenia.* Nature, 2010. **464**(7289): p. 763-7.
4. Hultman, R., et al., *Brain-wide Electrical Spatiotemporal Dynamics Encode Depression Vulnerability.* Cell, 2018. **173**(1): p. 166-180 e14.
5. Wang, X., et al., *Altered mGluR5-Homer scaffolds and corticostriatal connectivity in a Shank3 complete knockout model of autism.* Nat Commun, 2016. **7**: p. 11459.

6. Carlson, D., et al., *Dynamically Timed Stimulation of Corticolimbic Circuitry Activates a Stress-Compensatory Pathway.* Biol Psychiatry, 2017. **82**(12): p. 904-913.
7. Alcami, P. and A.E. Pereda, *Beyond plasticity: the dynamic impact of electrical synapses on neural circuits.* Nat Rev Neurosci, 2019. **20**(5): p. 253-271.
8. Sohl, G. and K. Willecke, *An update on connexin genes and their nomenclature in mouse and man.* Cell Commun Adhes, 2003. **10**(4-6): p. 173-80.
9. Sohl, G. and K. Willecke, *Gap junctions and the connexin protein family.* Cardiovasc Res, 2004. **62**(2): p. 228-32.
10. Laird, D.W., *Life cycle of connexins in health and disease.* Biochem J, 2006. **394**(Pt 3): p. 527-43.
11. Koval, M., S.A. Molina, and J.M. Burt, *Mix and match: investigating heteromeric and heterotypic gap junction channels in model systems and native tissues.* FEBS Lett, 2014. **588**(8): p. 1193-204.
12. Rash, J.E., et al., *Molecular and functional asymmetry at a vertebrate electrical synapse.* Neuron, 2013. **79**(5): p. 957-69.
13. O'Brien, J., et al., *Cloning and expression of two related connexins from the perch retina define a distinct subgroup of the connexin family.* J Neurosci, 1998. **18**(19): p. 7625-37.
14. Gong, X.Q., et al., *A mechanism of gap junction docking revealed by functional rescue of a human-disease-linked connexin mutant.* J Cell Sci, 2013. **126**(Pt 14): p. 3113-20.
15. Ransey, E., et al., *FETCH: A platform for high-throughput quantification of gap junction hemichannel docking.* BioRxiv, 2021.
16. Jordan, K., et al., *The origin of annular junctions: a mechanism of gap junction internalization.* J Cell Sci, 2001. **114**(Pt 4): p. 763-73.
17. Falk, M.M., et al., *Molecular mechanisms regulating formation, trafficking and processing of annular gap junctions.* BMC Cell Biol, 2016. **17 Suppl 1**: p. 22.
18. Li, X., et al., *Connexin45-containing neuronal gap junctions in rodent retina also contain connexin36 in both apposing hemiplaques, forming bihomotypic gap junctions, with scaffolding contributed by zonula occludens-1.* J Neurosci, 2008. **28**(39): p. 9769-89.
19. Condorelli, D.F., et al., *Expression of Cx36 in mammalian neurons.* Brain Res Brain Res Rev, 2000. **32**(1): p. 72-85.
20. Rash, J.E., et al., *Cell-specific expression of connexins and evidence of restricted gap junctional coupling between glial cells and between neurons.* J Neurosci, 2001. **21**(6): p. 1983-2000.
21. Hedgecock, E.M. and R.L. Russell, *Normal and mutant thermotaxis in the nematode Caenorhabditis elegans.* Proc Natl Acad Sci U S A, 1975. **72**(10): p. 4061-5.
22. Mori, I. and Y. Ohshima, *Neural regulation of thermotaxis in Caenorhabditis elegans.* Nature, 1995. **376**(6538): p. 344-8.
23. Hawk, J.D., et al., *Integration of Plasticity Mechanisms within a Single Sensory Neuron of C. elegans Actuates a Memory.* Neuron, 2018. **97**(2): p. 356-367 e4.
24. Siapas, A.G., E.V. Lubenov, and M.A. Wilson, *Prefrontal phase locking to hippocampal theta oscillations.* Neuron, 2005. **46**(1): p. 141-51.
25. Fuchs, E.C., et al., *Recruitment of parvalbumin-positive interneurons determines hippocampal function and associated behavior.* Neuron, 2007. **53**(4): p. 591-604.
26. Wulff, P., et al., *Hippocampal theta rhythm and its coupling with gamma oscillations require fast inhibition onto parvalbumin-positive interneurons.* Proc Natl Acad Sci U S A, 2009. **106**(9): p. 3561-6.
27. Sohal, V.S., et al., *Parvalbumin neurons and gamma rhythms enhance cortical circuit performance.* Nature, 2009. **459**(7247): p. 698-702.
28. Dzirasa, K., et al., *Lithium ameliorates nucleus accumbens phase signaling dysfunction in a genetic mouse model of mania.* J Neurosci, 2010. **30**(48): p. 16314 –16323.

29. Yao, Y., et al., *Phase Coupled Firing of Prefrontal Parvalbumin Interneuron With High Frequency Oscillations.* Front Cell Neurosci, 2020. **14**: p. 610741.
30. Canolty, R.T., et al., *High gamma power is phase-locked to theta oscillations in human neocortex.* Science, 2006. **313**(5793): p. 1626-8.
31. Steru, L., et al., *The tail suspension test: a new method for screening antidepressants in mice.* Psychopharmacology (Berl), 1985. **85**(3): p. 367-70.
32. Iniguez, S.D., et al., *Social defeat stress induces depression-like behavior and alters spine morphology in the hippocampus of adolescent male C57BL/6 mice.* Neurobiol Stress, 2016. **5**: p. 54-64.
33. Ide, S., et al., *Reduced emotional and corticosterone responses to stress in mu-opioid receptor knockout mice.* Neuropharmacology, 2010. **58**(1): p. 241-7.
34. Maeda, S., et al., *Structure of the connexin 26 gap junction channel at 3.5 A resolution.* Nature, 2009. **458**(7238): p. 597-602.
35. Bennett, B.C., et al., *An electrostatic mechanism for Ca(2+)-mediated regulation of gap junction channels.* Nat Commun, 2016. **7**: p. 8770.
36. Deisseroth, K., *Optogenetics.* Nat Methods, 2011. **8**(1): p. 26-9.
37. Yizhar, O., et al., *Neocortical excitation/inhibition balance in information processing and social dysfunction.* Nature, 2011. **477**(7363): p. 171-8.
38. Armbruster, B.N., et al., *Evolving the lock to fit the key to create a family of G protein-coupled receptors potently activated by an inert ligand.* Proc Natl Acad Sci U S A, 2007. **104**(12): p. 5163-8.
39. Siegle, J.H. and M.A. Wilson, *Enhancement of encoding and retrieval functions through theta phase-specific manipulation of hippocampus.* Elife, 2014. **3**: p. e03061.
40. Shui, Y., et al., *Molecular basis of junctional current rectification at an electrical synapse.* Sci Adv, 2020. **6**(27): p. eabb3076.
41. Pagnin, D., et al., *Efficacy of ECT in depression: a meta-analytic review.* J ECT, 2004. **20**(1): p. 13-20.
42. Liu, Y., et al., *Meta-analysis comparing deep brain stimulation of the globus pallidus and subthalamic nucleus to treat advanced Parkinson disease.* J Neurosurg, 2014. **121**(3): p. 709-18.
43. Jassim, A., et al., *Engineered Cx40 variants increased docking and function of heterotypic Cx40/Cx43 gap junction channels.* J Mol Cell Cardiol, 2016. **90**: p. 11-20.
44. Merritt, C. and G. Seydoux, *Transgenic solutions for the germline.* WormBook : the online review of C. elegans biology, 2010: p. 1-21.
45. Chelur, D.S. and M. Chalfie, *Targeted cell killing by reconstituted caspases.* Proceedings of the National Academy of Sciences of the United States of America, 2007. **104**(7): p. 2283-2288.
46. Chen, T.W., et al., *Ultrasensitive fluorescent proteins for imaging neuronal activity.* Nature, 2013. **499**(7458): p. 295-300.
47. Rabinowitch, I., et al., *Rewiring neural circuits by the insertion of ectopic electrical synapses in transgenic C. elegans.* Nature Communications, 2014. **5**.
48. Mello, C. and A. Fire, *DNA Transformation*, in *Methods in Cell Biology*. 1995. p. 451-482.
49. Lee, L.D., *Deciphering the Rules of Cell-to-Cell Coupling by Molecular Modeling and Simulation.* PDXScholar, 2018.
50. Song, Y., et al., *High-resolution comparative modeling with RosettaCM.* Structure, 2013. **21**(10): p. 1735-42.
51. Waterhouse, A., et al., *SWISS-MODEL: homology modelling of protein structures and complexes.* Nucleic Acids Res, 2018. **46**(W1): p. W296-W303.
52. Bertoni, M., et al., *Modeling protein quaternary structure of homo- and hetero-oligomers beyond binary interactions by homology.* Sci Rep, 2017. **7**(1): p. 10480.

53. Roy, A., A. Kucukural, and Y. Zhang, *I-TASSER: a unified platform for automated protein structure and function prediction.* Nat Protoc, 2010. **5**(4): p. 725-38.
54. Yang, J., et al., *The I-TASSER Suite: protein structure and function prediction.* Nat Methods, 2015. **12**(1): p. 7-8.
55. Yang, J. and Y. Zhang, *I-TASSER server: new development for protein structure and function predictions.* Nucleic Acids Res, 2015. **43**(W1): p. W174-81.
56. Kelley, L.A., et al., *The Phyre2 web portal for protein modeling, prediction and analysis.* Nat Protoc, 2015. **10**(6): p. 845-58.
57. Kallberg, M., et al., *Template-based protein structure modeling using the RaptorX web server.* Nat Protoc, 2012. **7**(8): p. 1511-22.
58. Yang, Y., et al., *Improving protein fold recognition and template-based modeling by employing probabilistic-based matching between predicted one-dimensional structural properties of query and corresponding native properties of templates.* Bioinformatics, 2011. **27**(15): p. 2076-82.
59. Davis, I.W., et al., *MolProbity: all-atom contacts and structure validation for proteins and nucleic acids.* Nucleic Acids Res, 2007. **35**(Web Server issue): p. W375-83.
60. Chen, V.B., et al., *MolProbity: all-atom structure validation for macromolecular crystallography.* Acta Crystallogr D Biol Crystallogr, 2010. **66**(Pt 1): p. 12-21.
61. Williams, C.J., et al., *MolProbity: More and better reference data for improved all-atom structure validation.* Protein Sci, 2018. **27**(1): p. 293-315.
62. Myers, J.B., et al., *Structure of native lens connexin 46/50 intercellular channels by cryo-EM.* Nature, 2018. **564**(7736): p. 372-377.
63. Humphrey, W., A. Dalke, and K. Schulten, *VMD: visual molecular dynamics.* J Mol Graph, 1996. **14**(1): p. 33-8, 27-8.
64. Eargle, J., D. Wright, and Z. Luthey-Schulten, *Multiple Alignment of protein structures and sequences for VMD.* Bioinformatics, 2006. **22**(4): p. 504-6.
65. Jo, S., et al., *CHARMM-GUI: a web-based graphical user interface for CHARMM.* J Comput Chem, 2008. **29**(11): p. 1859-65.
66. Wu, E.L., et al., *CHARMM-GUI Membrane Builder toward realistic biological membrane simulations.* J Comput Chem, 2014. **35**(27): p. 1997-2004.
67. Jo, S., et al., *CHARMM-GUI Membrane Builder for mixed bilayers and its application to yeast membranes.* Biophys J, 2009. **97**(1): p. 50-8.
68. Jo, S., T. Kim, and W. Im, *Automated builder and database of protein/membrane complexes for molecular dynamics simulations.* PLoS One, 2007. **2**(9): p. e880.
69. Lee, J., et al., *CHARMM-GUI Membrane Builder for Complex Biological Membrane Simulations with Glycolipids and Lipoglycans.* J Chem Theory Comput, 2019. **15**(1): p. 775-786.
70. Alberts, B., *Molecular biology of the cell*. Sixth edition. ed. 2015, New York, NY: Garland Science, Taylor and Francis Group. 1 volume (various pagings).
71. Phillips, J.C., et al., *Scalable molecular dynamics with NAMD.* J Comput Chem, 2005. **26**(16): p. 1781-802.
72. Brenner, S., *The genetics of Caenorhabditis elegans.* Genetics, 1974. **77**(1): p. 71-94.
73. Luo, L., et al., *Bidirectional thermotaxis in Caenorhabditis elegans is mediated by distinct sensorimotor strategies driven by the AFD thermosensory neurons.* Proceedings of the National Academy of Sciences of the United States of America, 2014. **111**(7): p. 2776-2781.
74. Stiernagle, T., *Maintenance of C. elegans.* WormBook : the online review of C. elegans biology, 2006: p. 1-11.
75. Gershow, M., et al., *Controlling airborne cues to study small animal navigation.* Nature Methods, 2012. **9**(3): p. 290-296.

76. Edelstein, A.D., et al., *Advanced methods of microscope control using muManager software.* J Biol Methods, 2014. **1**(2).
77. Schindelin, J., et al., *Fiji: an open-source platform for biological-image analysis.* Nature Methods, 2012. **9**(7): p. 676-682.
78. Clark, D.A., et al., *The AFD sensory neurons encode multiple functions underlying thermotactic behavior in Caenorhabditis elegans.* Journal of Neuroscience, 2006. **26**(28): p. 7444-7451.
79. Mague, S.D., et al., *Brain-wide electrical dynamics encode an appetitive socioemotional state* BioRxiv, 2020.

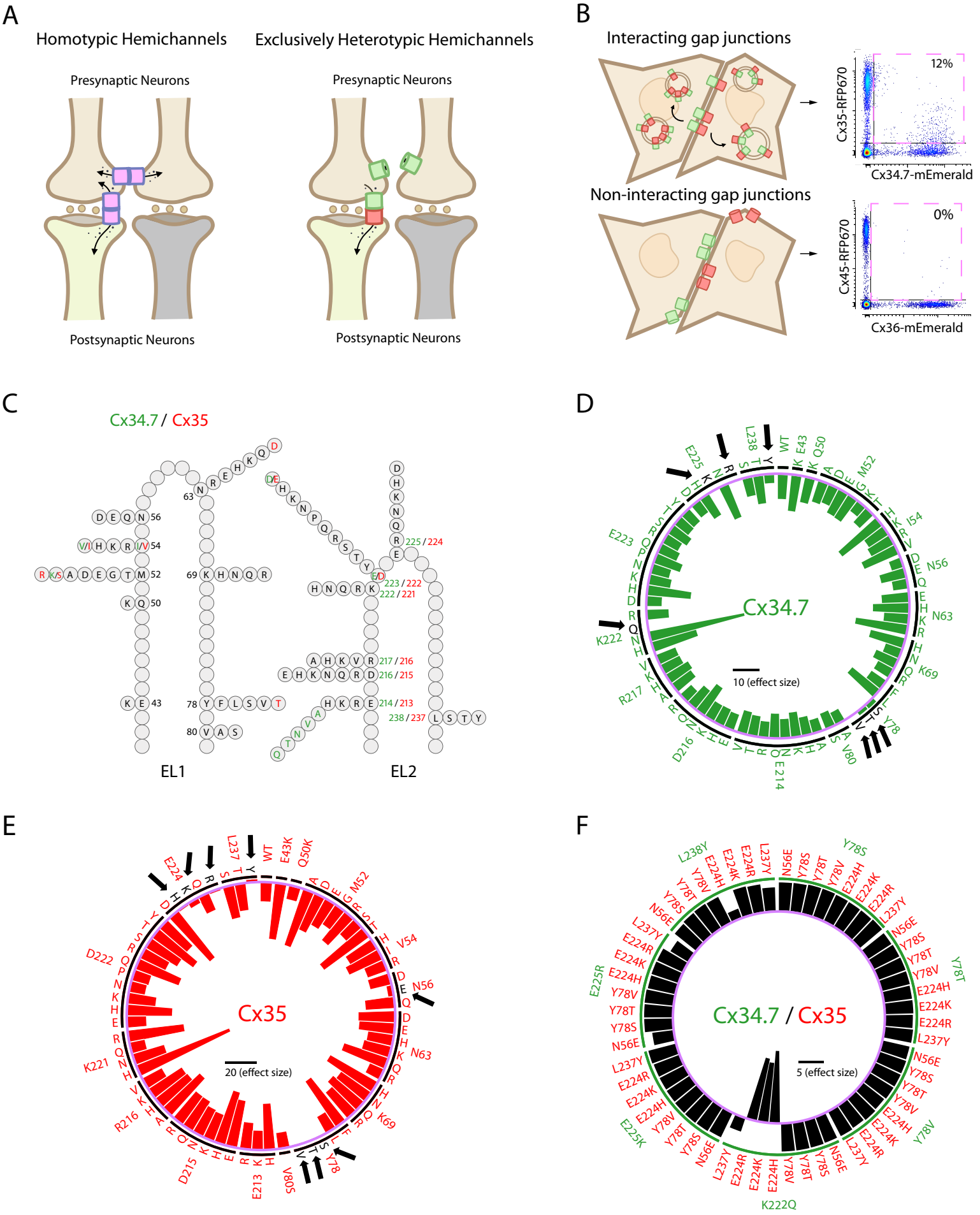
A
Homotypic Hemichannels
Exclusively Heterotypic Hemichannels
Presynaptic Neurons
Presynaptic Neurons
Postsynaptic Neurons
Postsynaptic Neurons
B
Interacting gap junctions
12%
Cx35-RFP670
Cx34.7-mEmerald
Non-interacting gap junctions
0%
Cx45-RFP670
Cx36-mEmerald
C
Cx34.7 / Cx35
EL1
EL2
D
Cx34.7
10 (effect size)
E
Cx35
20 (effect size)
F
Cx34.7 / Cx35
5 (effect size)

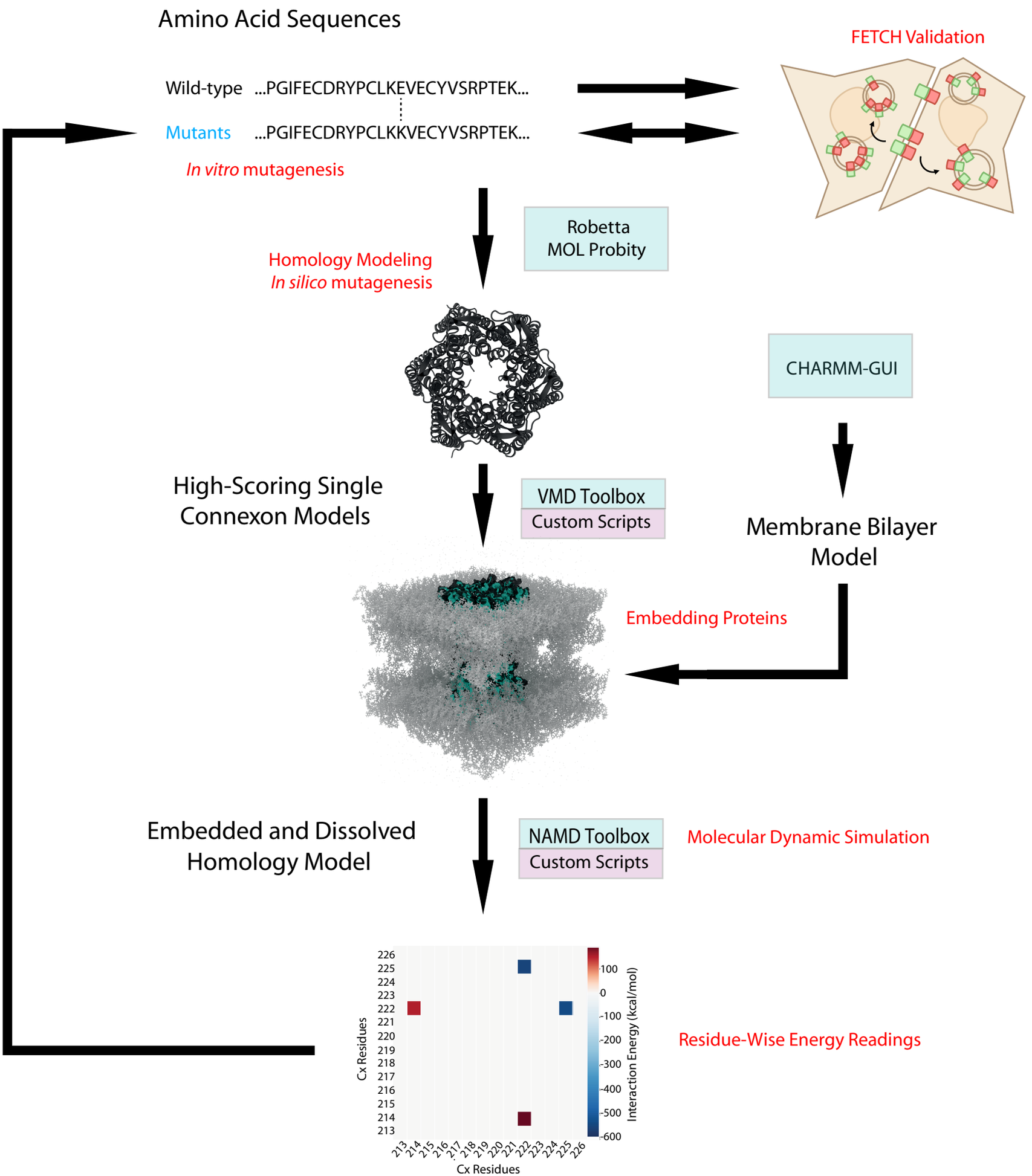
Amino Acid Sequences
Wild-type ...PGIFECDRYPCLKEVECYVSRPTEK...
Mutants ...PGIFECDRYPCLKKVECYVSRPTEK...
In vitro mutagenesis
FETCH Validation
Robetta
MOL Probity
Homology Modeling
In silico mutagenesis
CHARMM-GUI
High-Scoring Single Connexon Models
VMD Toolbox
Custom Scripts
Membrane Bilayer Model
Embedding Proteins
Embedded and Dissolved Homology Model
NAMD Toolbox
Custom Scripts
Molecular Dynamic Simulation
Cx Residues
Cx Residues
Interaction Energy (kcal/mol)
Residue-Wise Energy Readings

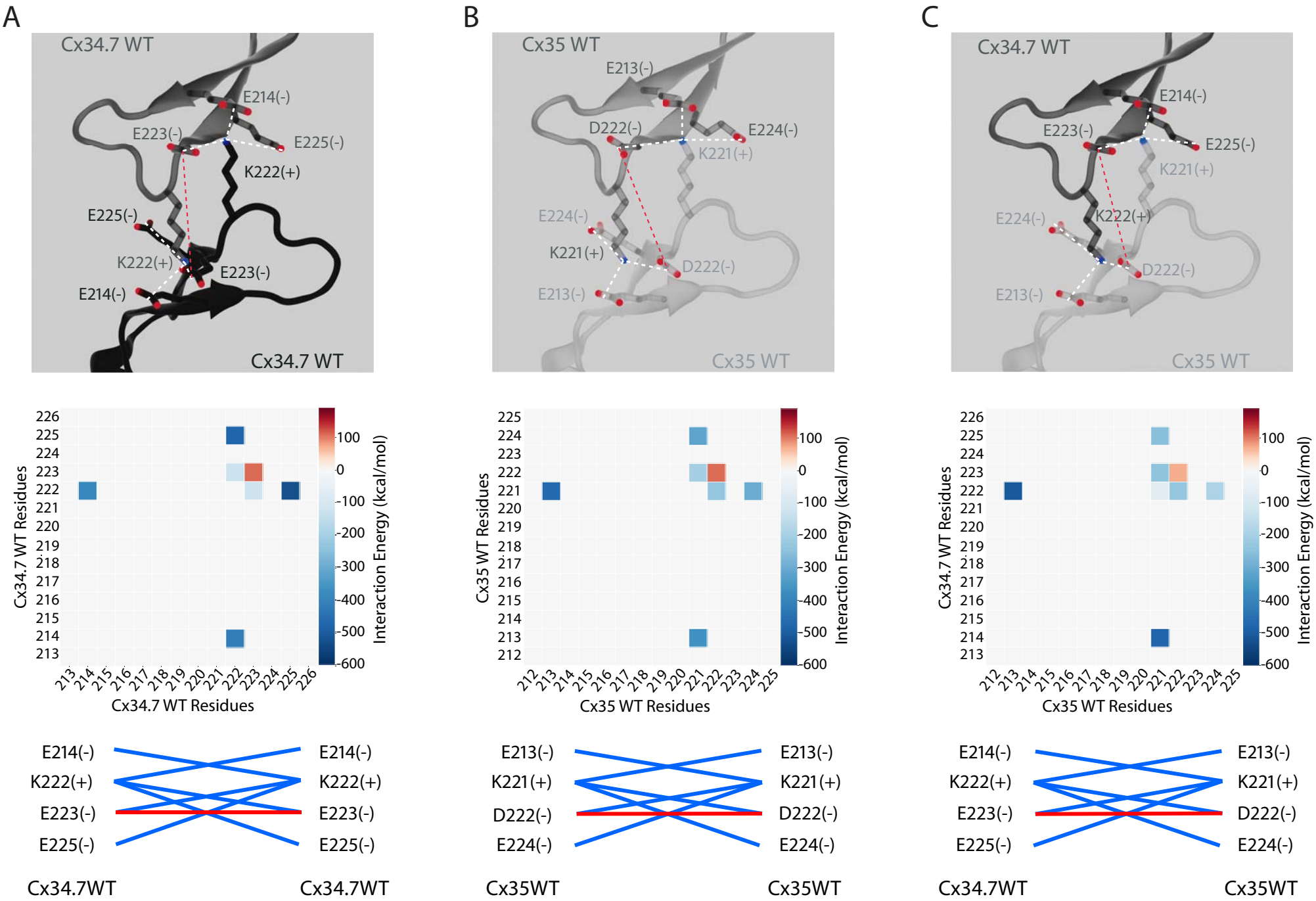
A
Cx34.7 WT
E214(-)
E223(-)
E225(-)
K222(+)
E225(-)
K222(+)
E223(-)
E214(-)
Cx34.7 WT
B
Cx35 WT
E213(-)
D222(-)
E224(-)
K221(+)
E224(-)
K221(+)
D222(-)
E213(-)
Cx35 WT
C
Cx34.7 WT
E214(-)
E223(-)
E225(-)
K221(+)
E224(-)
K222(+)
D222(-)
E213(-)
Cx35 WT
Cx34.7 WT Residues
Cx35 WT Residues
Interaction Energy (kcal/mol)
E214(-)
K222(+)
E223(-)
E225(-)
Cx34.7WT
Cx34.7WT
E213(-)
K221(+)
D222(-)
E224(-)
Cx35WT
Cx35WT
E214(-)
K222(+)
E223(-)
E225(-)
Cx34.7WT
E213(-)
K221(+)
D222(-)
E224(-)
Cx35WT

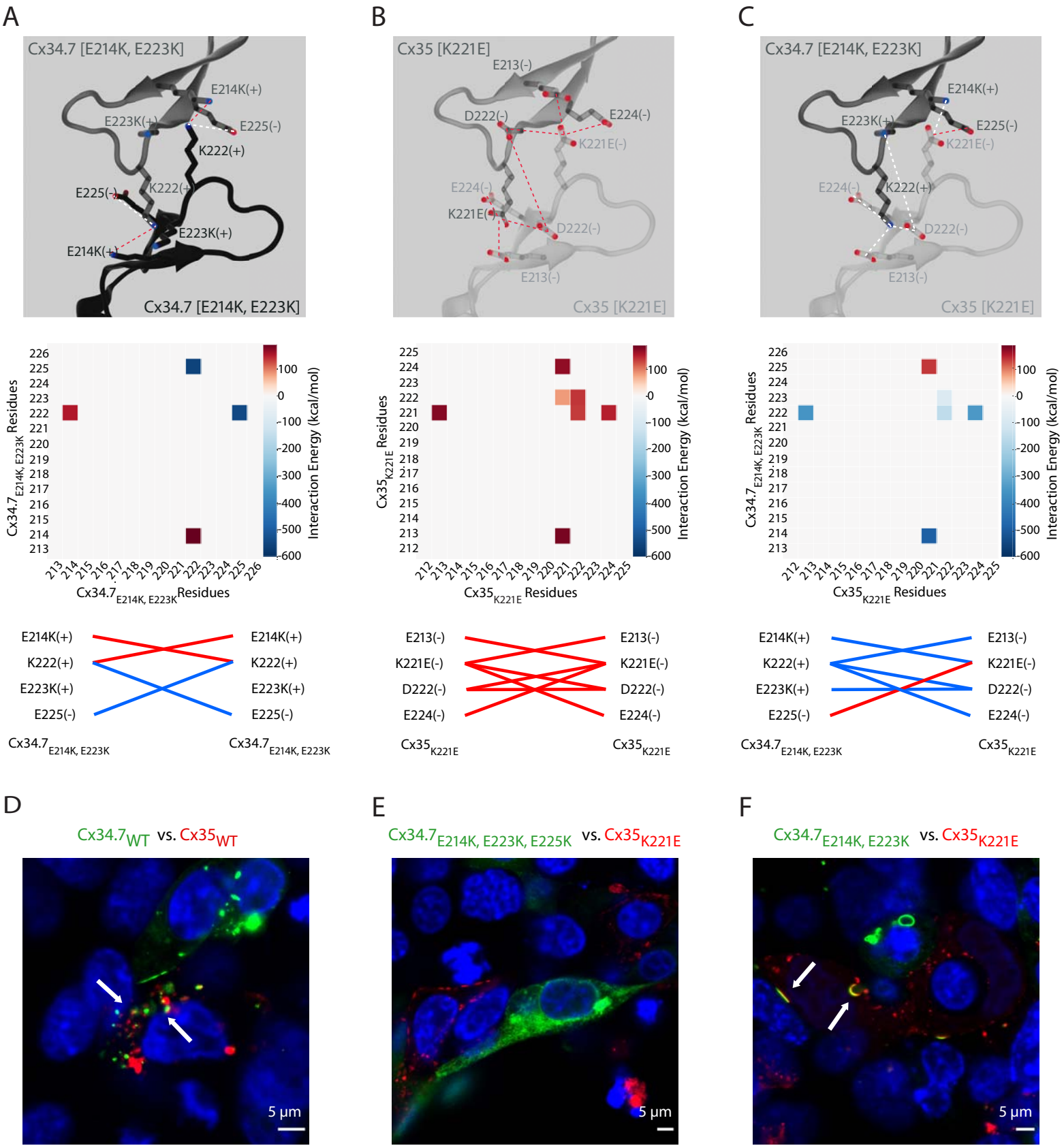
A
Cx34.7 [E214K, E223K]
E214K(+)
E223K(+)
E225(-)
K222(+)
E225(-)
K222(+)
E223K(+)
E214K(+)
Cx34.7 [E214K, E223K]
B
Cx35 [K221E]
E213(-)
D222(-)
E224(-)
K221E(-)
E224(-)
K221E(-)
D222(-)
E213(-)
Cx35 [K221E]
C
Cx34.7 [E214K, E223K]
E214K(+)
E223K(+)
E225(-)
K221E(-)
E224(-)
K222(+)
D222(-)
E213(-)
Cx35 [K221E]
Cx34.7 E214K, E223K Residues
Interaction Energy (kcal/mol)
Cx35 K221E Residues
E214K(+)
K222(+)
E223K(+)
E225(-)
Cx34.7 E214K, E223K
E213(-)
K221E(-)
D222(-)
E224(-)
Cx35 K221E
D
Cx34.7 WT vs. Cx35 WT
5 µm
E
Cx34.7 E214K, E223K, E225K vs. Cx35 K221E
5 µm
F
Cx34.7 E214K, E223K vs. Cx35 K221E
5 µm

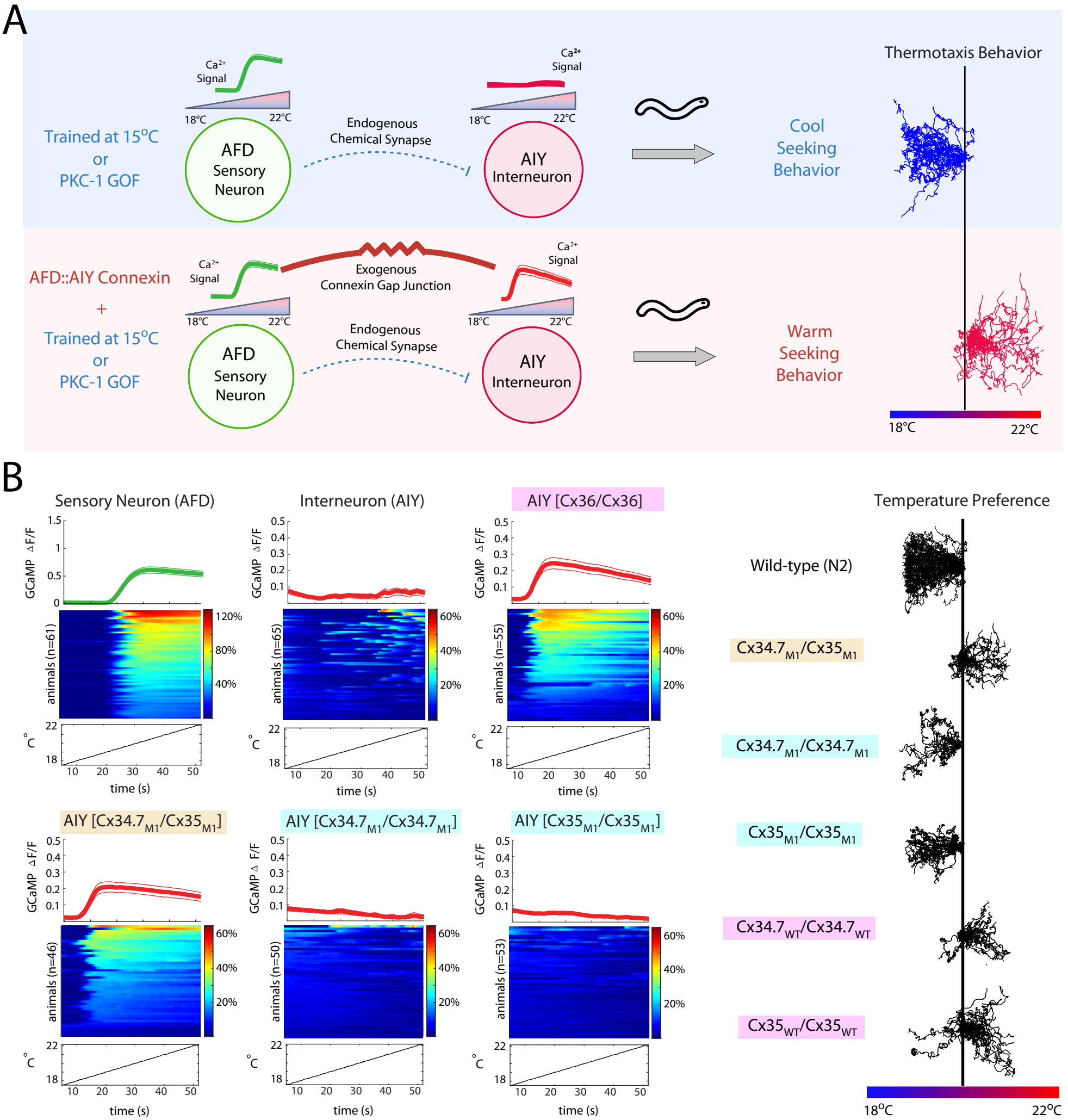
A
Trained at 15°C
or
PKC-1 GOF
Ca2+ Signal
18°C
22°C
AFD
Sensory
Neuron
Endogenous
Chemical Synapse
AIY
Interneuron
Cool
Seeking
Behavior
Thermotaxis Behavior
AFD::AIY Connexin
+
Trained at 15°C
or
PKC-1 GOF
Exogenous
Connexin Gap Junction
Warm
Seeking
Behavior
B
Sensory Neuron (AFD)
Interneuron (AIY)
AIY [Cx36/Cx36]
AIY [Cx34.7M1/Cx35M1]
AIY [Cx34.7M1/Cx34.7M1]
AIY [Cx35M1/Cx35M1]
GCaMP ΔF/F
animals (n=61)
animals (n=65)
animals (n=55)
animals (n=46)
animals (n=50)
animals (n=53)
°C
time (s)
Temperature Preference
Wild-type (N2)
Cx34.7M1/Cx35M1
Cx34.7M1/Cx34.7M1
Cx35M1/Cx35M1
Cx34.7WT/Cx34.7WT
Cx35WT/Cx35WT
18°C
22°C
C
Response Penetrance
(% Animals Responding)
Sensory Neuron (AFD)
Interneuron (AIY)
Cx36/Cx36
Cx34.7M1/Cx35M1
Cx34.7M1/Cx34.7M1
Cx35M1/Cx35M1
Cx34.7WT/Cx34.7WT
Cx35WT/Cx35WT
Cx Configuration (AFD::AIY)
D
TTX Index
N2
olals17
Cx36/Cx36
Cx34.7M1/Cx35M1
Cx34.7M1/Cx34.7M1
Cx35M1/Cx35M1
Cx34.7WT/Cx34.7WT
Cx35WT/Cx35WT
Cx Configuration (AFD::AIY)

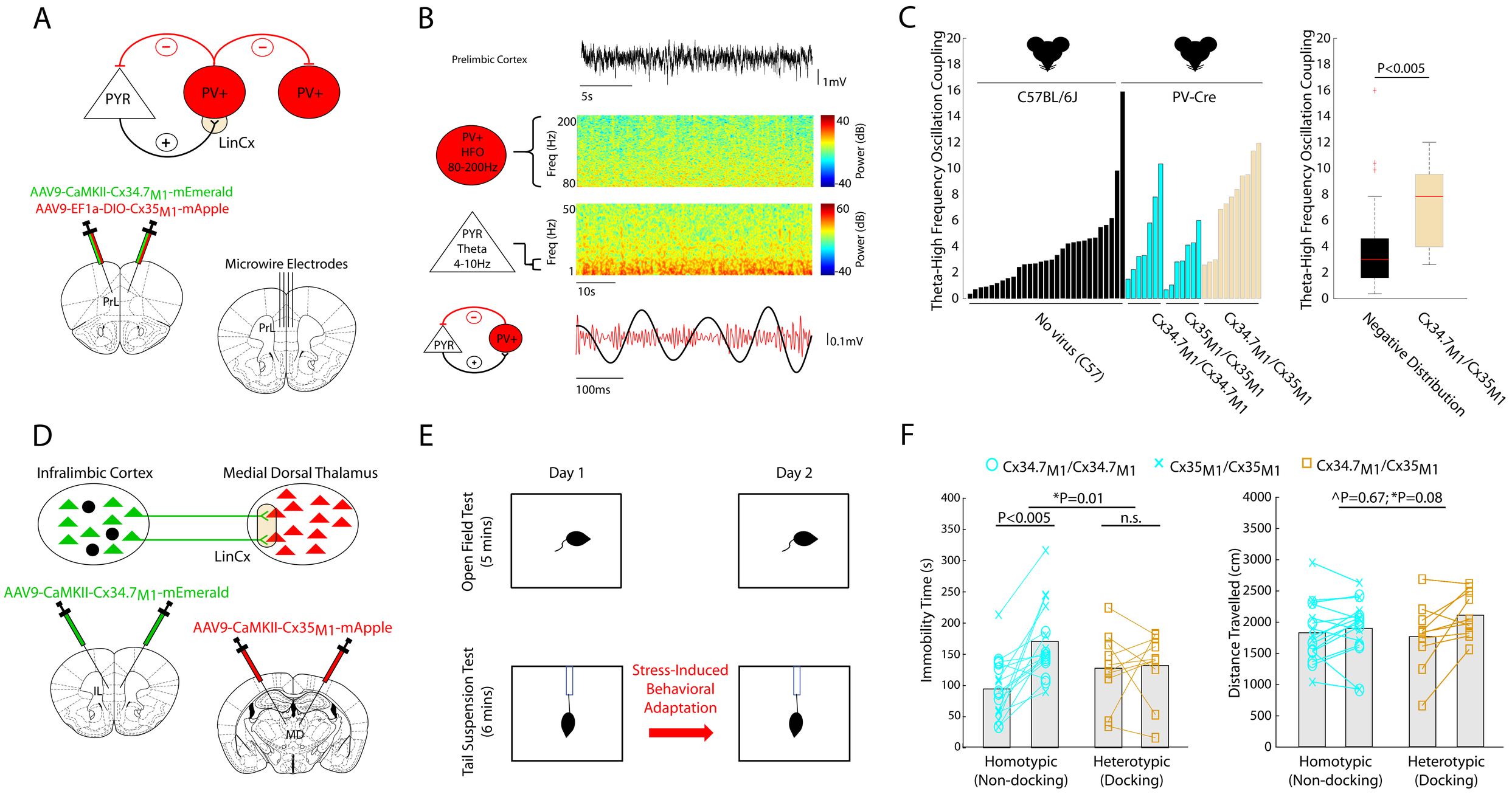
A
PYR
PV+
PV+
LinCx
AAV9-CaMKII-Cx34.7M1-mEmerald
AAV9-EF1a-DIO-Cx35M1-mApple
PrL
Microwire Electrodes
PrL
B
Prelimbic Cortex
1mV
5s
PV+
HFO
80-200Hz
Freq (Hz)
200
80
40
-40
Power (dB)
PYR
Theta
4-10Hz
Freq (Hz)
50
1
60
-40
Power (dB)
10s
PYR
PV+
0.1mV
100ms
C
Theta-High Frequency Oscillation Coupling
C57BL/6J
PV-Cre
No virus (C57)
Cx34.7M1/Cx34.7M1
Cx35M1/Cx35M1
Cx34.7M1/Cx35M1
P<0.005
Negative Distribution
Cx34.7M1/Cx35M1
D
Infralimbic Cortex
Medial Dorsal Thalamus
LinCx
AAV9-CaMKII-Cx34.7M1-mEmerald
AAV9-CaMKII-Cx35M1-mApple
IL
MD
E
Day 1
Day 2
Open Field Test
(5 mins)
Tail Suspension Test
(6 mins)
Stress-Induced
Behavioral
Adaptation
F
Cx34.7M1/Cx34.7M1
Cx35M1/Cx35M1
Cx34.7M1/Cx35M1
Immobility Time (s)
*P=0.01
P<0.005
n.s.
Homotypic
(Non-docking)
Heterotypic
(Docking)
Distance Travelled (cm)
^P=0.67; *P=0.08
Homotypic
(Non-docking)
Heterotypic
(Docking)